ISSN 1831-9424

Advanced Radiative Transfer Models for the simulation of In situ and Satellite Ocean Color data (ARTEMIS-OC):

the Novel Adjacency Perturbation Simulator for Coastal Areas (NAUSICAA) code

Bulgarelli, B., D'Alimonte, D., Kajiyama, T.

2025

Joint
Research
Centre

EUR 40238

This document is a publication by the Joint Research Centre (JRC), the European Commission's science and knowledge service. It aims to provide evidence-based scientific support to the European policymaking process. The contents of this publication do not necessarily reflect the position or opinion of the European Commission. Neither the European Commission nor any person acting on behalf of the Commission is responsible for the use that might be made of this publication. For information on the methodology and quality underlying the data used in this publication for which the source is neither Eurostat nor other Commission services, users should contact the referenced source. The designations employed and the presentation of material on the maps do not imply the expression of any opinion whatsoever on the part of the European Union concerning the legal status of any country, territory, city or area or of its authorities, or concerning the delimitation of its frontiers or boundaries.

Contact information
Name: Barbara Bulgarelli
Address: European Commission, Joint Research Centre (JRC), Ispra, Italy
Email: barbara.bulgarelli(at)ec.europa.eu

EU Science Hub
https://joint-research-centre.ec.europa.eu
JRC141105

EUR 40238

PDF ISBN 978-92-68-24989-5 ISSN 1831-9424 doi:10.2760/1597600 KJ-01-25-107-EN-N

Luxembourg: Publications Office of the European Union, 2025

© European Union, 2025

The reuse policy of the European Commission documents is implemented by the Commission Decision 2011/833/EU of 12 December 2011 on the reuse of Commission documents (OJ L 330, 14.12.2011, p. 39). Unless otherwise noted, the reuse of this document is authorised under the Creative Commons Attribution 4.0 International (CC BY 4.0) licence (https://creativecommons.org/licenses/by/4.0/). This means that reuse is allowed provided appropriate credit is given and any changes are indicated.

For any use or reproduction of photos or other material that is not owned by the European Union permission must be sought directly from the copyright holders.

How to cite this report: European Commission: Joint Research Centre, Bulgarelli, B., D`Alimonte, D. and Kajiyama, T., *Advanced Radiative Transfer Models for the simulation of In situ and Satellite Ocean Color data (ARTEMIS-OC): the Novel Adjacency Perturbation Simulator for Coastal Areas (NAUSICAA) code,* Publications Office of the European Union, Luxembourg, 2025, https://data.europa.eu/doi/10.2760/1597600, JRC141105.

Contents

Abstract

This report, the second in a series, leverages JRC extensive experience in developing and applying highly accurate radiative transfer models to simulate *in situ* and satellite aquatic data, which are integrated into the JRC's Advanced Radiative Transfer Models for In situ and Satellite Ocean Color data (ARTEMIS-OC) software suite.

ARTEMIS-OC includes *i*) the FEM code for simulating unpolarised solar radiation in open-ocean environments, *ii*) the PERSEA code to ensure a flexible and comprehensive modelling of the optical properties of realistic atmosphere and water environments, *iii*) the SkyFEM, FEMrad-OC, and AquaFEM codes, which are tailored FEM-PERSEA configurations to reproduce the sky-radiance distribution and the radiance detected by satellite and in-water sensors, respectively; and *iv*) the NAUSICAA code to simulate unpolarised solar radiation in coastal and inland water regions, i.e., in the presence of nearby land perturbations.

All algorithms account for multiple scattering and allow varying illumination and observation geometries.

The present report focuses on the NAUSICAA code and its applications in investigating and reducing uncertainties in OC data products.

The ultimate goal of this report series is to provide a comprehensive description of the ARTEMIS-OC simulation tools in support of the Copernicus Programme launched in 2014 to establish a European capacity for Earth Observation.

Foreword

Ocean Color (OC) is the apparent hue of the water resulting from its interactions with the sunlight.

Waters cover more than 70% of the Earth's surface, and Earth Observation (EO) data derived from OC remote sensing are essential to monitor water quality, manage aquatic resources and quantify the impact of climate change.

OC data products are indeed recognised by the Global Ocean Observing System (GOOS) and the Global Climate Observation System (GCOS) as critical for monitoring ocean health and climate change.

Within the Copernicus Program, launched in 2014 to establish a European capacity for EO (Regulation EU No377/2014), both the Marine Environment Monitoring Service (CMEMS), the Climate Change Service (C3S) and the Land Monitoring Service (CLMS) rely on OC data products, like the radiance (or the reflectance) leaving the water bodies and the Chlorophyll-a concentration (used as a proxy for phytoplankton biomass).

Understanding and quantifying uncertainties associated with OC data products is thus crucial for environmental and climate applications, as well as for their use in the anticipation, definition, implementation and monitoring of the EU Water Acquis and Marine legislation.

Theoretical radiative transfer models (RTMs) capable to simulate the global optical signal at *in situ* and satellite sensors, as well as its individual components, offer a powerful tool for evaluating uncertainties affecting optical data products: by bridging the gap between observations and physical processes, modelling provides a unique framework for identifying and analysing the various sources of perturbations that impact satellite and *in situ* data.

JRC has multi-decadal expertise in the development and application of highly accurate RTMs for the simulation of OC satellite and *in situ* data, now incorporated into the Advanced Radiative Transfer Models for In situ and Satellite Ocean Color data (ARTEMIS-OC) software suite, which includes:

- The Finite Element Method (FEM) code, for simulating unpolarised solar radiation in open-ocean environments;
- The Propagating Environment for Radiance Simulations in atmosphEre and wAter (PERSEA) code, to ensure a flexible and comprehensive modelling of the optical properties of realistic atmosphere and water environments;
- The SkyFEM code, tailored to simulate the distribution of the sky radiance;
- The FEMrad-OC code, facilitating a comprehensive simulation of the signal received by satellite OC sensors;
- The AquaFEM code, enabling the simulation of radiance distribution and apparent optical properties within and just above natural water bodies;
- The Novel Adjacency Perturbation Simulator for Coastal Areas (NAUSICAA) code, to explore perturbations induced by nearby land surfaces in OC data from coastal or inland waters, the so-called *adjacency effects* (AE).

While FEM is a one-dimensional deterministic numerical code, NAUSICAA is a stochastic three-dimensional one. SkyFEM, FEMrad-OC, and AquaFEM are specific configurations of the coupled FEM-PERSEA codes.

ARTEMIS-OC models adhere to the five principles delineated in the manifesto for best practices in responsible mathematical modelling (Saltelli et al., 2020), carefully taking into consideration assumptions, hubris, framing, consequences, and unknowns.

The present report describes the NAUSICAA code.

NAUSICAA has been extensively applied to investigate *adjacency effects* in OC remote sensing data from inland and coastal water regions, with specific reference to Sentinel-2 and -3 Copernicus data.

NAUSICAA results were used in support to the definition of the Committee on Earth Observation Satellites (CEOS) Analysis Ready Data (ARD) for aquatic reflectance (Siqueira et al., 2022), and to the establishment of a European system vicarious calibration (SVC) infrastructure for satellite OC sensors (Bulgarelli and Zibordi, 2020).

Acknowledgements

The content of this report summarises results published in peer-review literature by the authors in collaboration with a number of colleagues whose contribution is duly acknowledged. Specifically, grateful thanks are due to: dr. Viatchelsav Kiselev, former EOMAP GmbH and Co., dr. Giuseppe Zibordi (NASA GSFC & University of Maryland Baltimore County, former JRC), and dr. J-F. Berthon (JRC).

This report is a contribution to *Earth Observation Knowledge, Innovation Science and Services* (EOKISS) funded by the Joint Research Centre (JRC).

The support provided by DG DEFIS (the European Commission Directorate-General for Defence Industry and Space) and the Copernicus Programme is also gratefully acknowledged.

Authors

Barbara Bulgarelli, European Commission, Joint Research Centre (JRC), Ispra, Italy

Davide D’Alimonte, AEQUORA, Lisbon, Portugal

Tamito Kajiyama, AEQUORA, Lisbon, Portugal

1 Introduction

This report is the second in a series to illustrate JRC extensive capacities in developing and applying highly accurate radiative transfer models (RTMs) for the simulation of *in situ* and satellite aquatic data, integral part the JRC's Advanced Radiative Transfer Models for In situ and Satellite Ocean Color data (ARTEMIS-OC) software suite.

RTMs play a crucial role in deciphering the information collected by satellite and *in situ* sensors, and in assessing the quality of derived data products.

RTMs are capable to theoretically reproduce the journey of the solar radiation within the Earth environment and up to the optical sensor, thus establishing the most rational connection between observations and physical processes.

Apt to theoretically quantify the distinct radiance contributions at the sensor, RTMs further allow a wide-ranging analysis of the perturbations affecting field and satellite measurements in support of the development, implementation, assessment and refinement of correction schemes and protocols for satellite and *in situ* measurements.

Any RTM can be considered as the coupling of a core algorithm to solve the mathematical equation describing the transferring of the radiation (the so-called *radiative transfer equation*, RTE) with a parametric modelling of the medium where the radiance propagates (i.e., the *propagating system*, see Fig. 1).

The accuracy of the RTM hence depends on a correct, accurate and efficient mathematical solution of the RTE, and a correct and accurate characterisation of the propagating system.

Figure 1. Scheme of an RTM, as composed by a core algorithm for the mathematical solution of the RTE and a parametric modelling of the propagating system

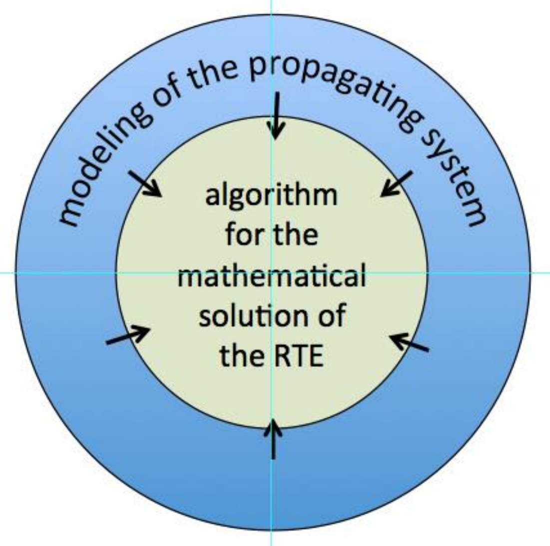

Source:(Bulgarelli, 2023)

The present report specifically focuses on the Novel Adjacency Perturbation Simulator for Coastal Areas (NAUSICAA), which is a powerful and accurate backward Monte Carlo (MC) code for the numerical solution of the RTE in a three-dimensional medium, developed and successfully applied to investigate perturbations induced by nearby land in OC data from coastal and inland water regions, the so-called *adjacent effects* (Bulgarelli et al., 2018, 2017, 2014; Bulgarelli and Zibordi, 2020, 2018a, 2018b)

Section 1.1 briefly presents the ARTEMIS-OC software suite; Section 1.2 introduces the concept of adjacency effects and their quantification; Section 1.3 provides a general overview of the Monte Carlo methodology.

Section 2 describes the NAUSICAA code, including the implemented mathematical method, its accuracy and validation, as well as its data inputs and outputs. Most relevant NAUSICAA applications are summarised in Section 3. Conclusions are drawn in Section 4.

1.1 The ARTEMIS-OC software suite

ARTEMIS-OC, which stands for Advanced Radiative Transfer Models for In situ and Satellite Ocean Color data, is a JRC software suite including a variety of RTMs enabling the simulation of the total unpolarised radiance at satellite and *in situ* Ocean Color (OC) sensors (as well as its distinct components) at any visible and near-infrared (NIR) center-wavelength, and for any illumination and observation geometry (Fig. 2).

Figure 2. ARTEMIS-OC modelling capabilities: a) modelling of satellite ocean color data, b) modelling of in-situ ocean color data, c) system characteristics which are accounted for.

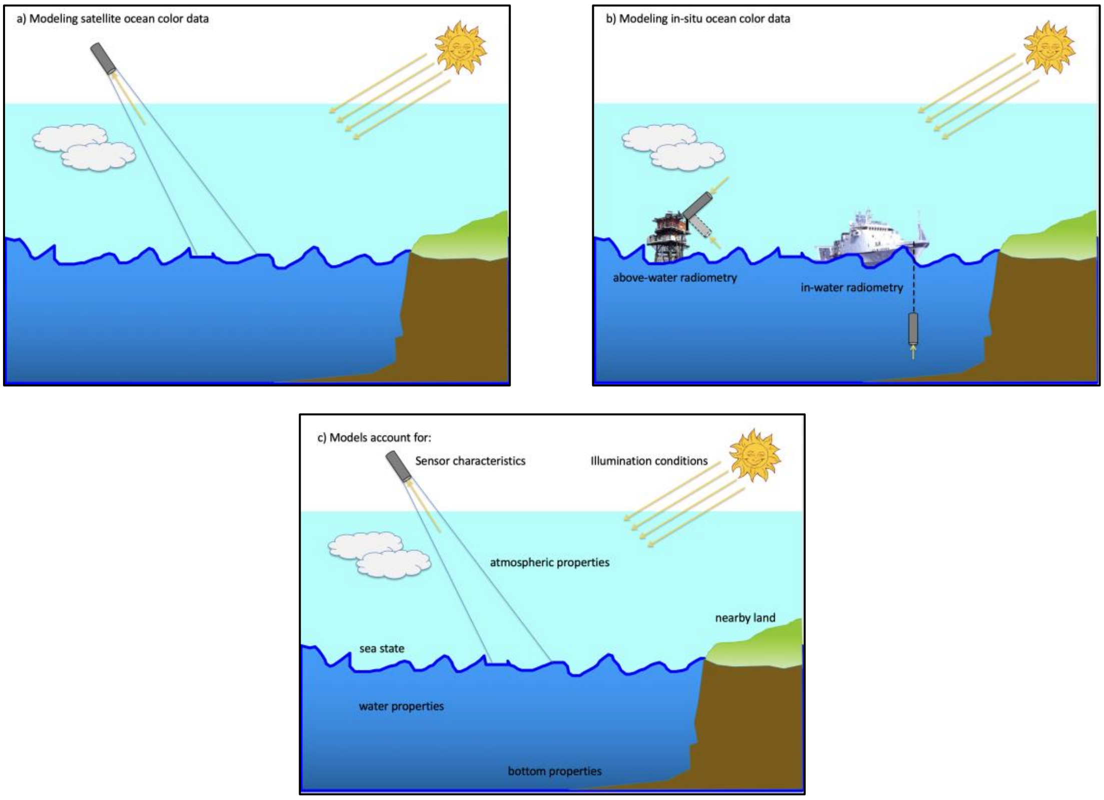

Source: (Bulgarelli et al., 2025)

The ARTEMIS-OC software suite comprises:

- the Finite Element Method (FEM) numerical code: to simulate unpolarised radiance transport in a plane-parallel system with a change in the refractive index (like the atmosphere-ocean system);
- the Propagating Environment for Radiance Simulations in atmosphEre and wAter (PERSEA) code: to model the optical properties of atmosphere and water accounting for realistic bio-geophysical conditions.
- SkyFEM: to model the sky-radiance distribution;
- FEMrad-OC: to reproduce the signal received by satellite OC sensors;
- AquaFEM: to simulate the radiance distributions and apparent optical properties within and just above any natural water body;
- the Novel Adjacency Perturbation Simulator for Coastal Areas (NAUSICAA): to investigate adjacency perturbations induced by nearby land in OC data from coastal regions or inland water basins.

FEM (Bulgarelli et al., 1999; Kisselev et al., 1995; Bulgarelli, 2024) implements a highly accurate deterministic numerical algorithm based on the finite element method (Fig. 3). SkyFEM, FEMrad-OC and AquaFEM are targeted configurations of the coupled FEM-PERSEA codes (Fig. 4 and 5). NAUSICAA (Bulgarelli et al., 2014) is a stochastic three-dimensional (3D) MC code designed for simulating the propagation of unpolarised solar radiation in an atmospheric medium bounded by an inhomogeneous reflecting surface, as depicted in Fig. 6. This configuration is particularly relevant for coastal or inland water regions.

All the algorithms account for multiple interactions within the propagating system and allow considering varying illumination and observation geometries.

Figure 3. Scheme of the FEM code for the solution of the RTE

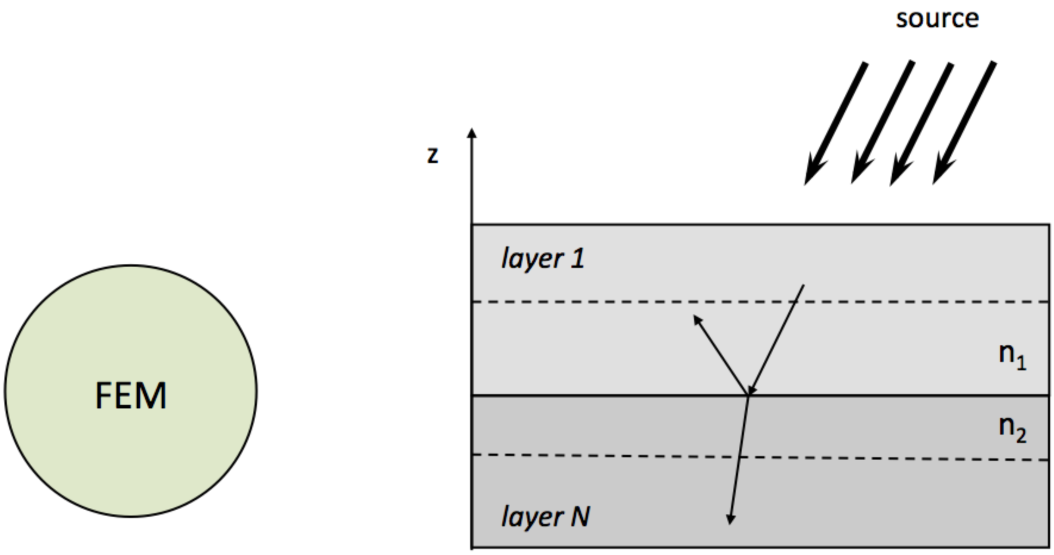

Source:(Bulgarelli, 2023)

Figure 4. Scheme for the modelling of the propagating system in PERSEA

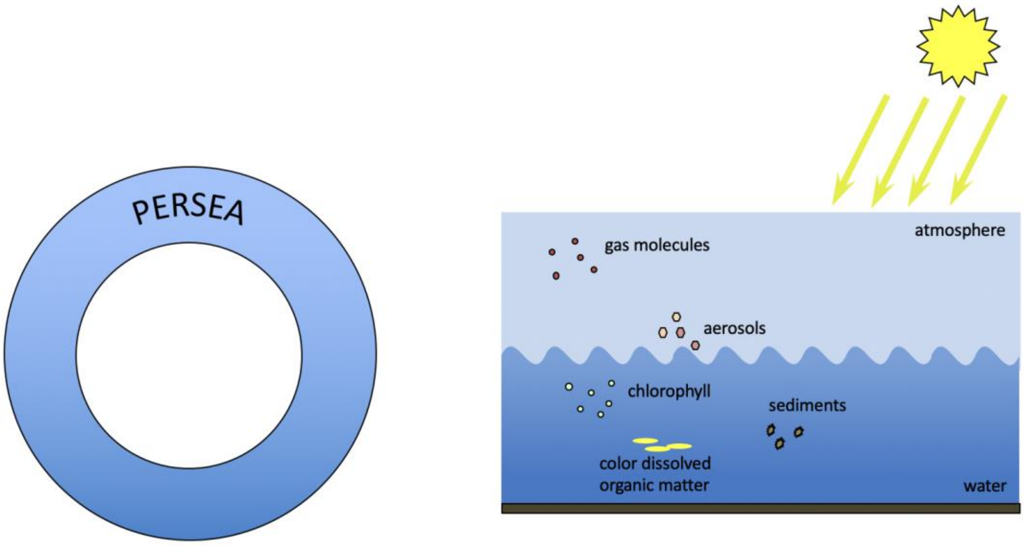

Source: (Bulgarelli et al., 2025)

Figure 5. Scheme for SkyFEM, FEMrad-OC and AquaFEM

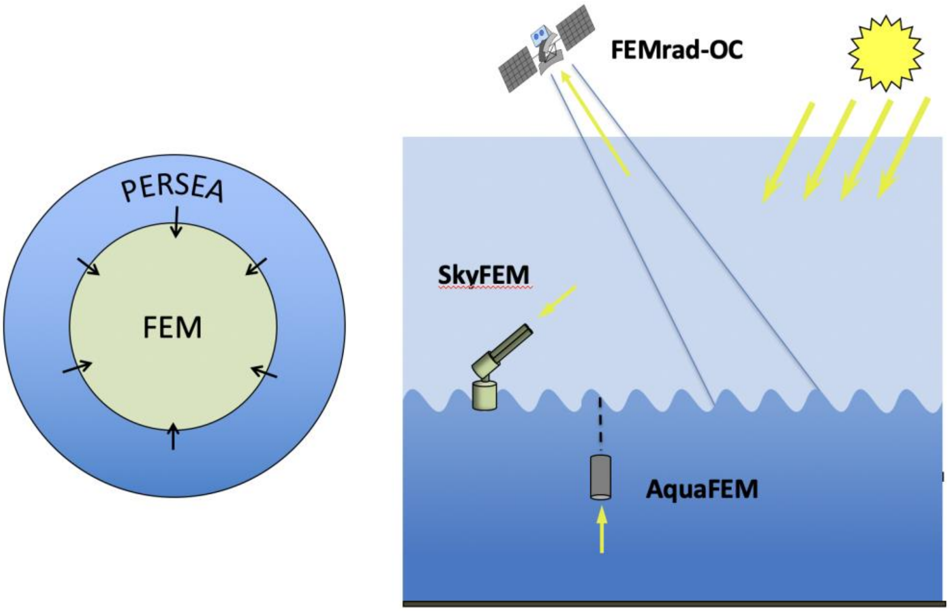

Source: (Bulgarelli et al., 2025)

Figure 6. Scheme for NAUSICAA

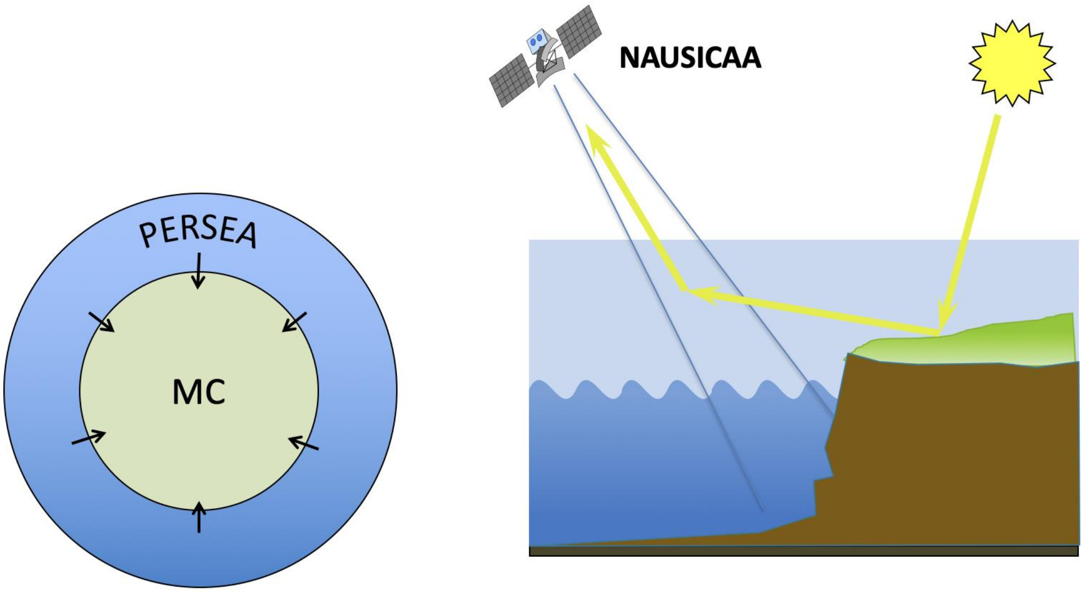

Source: (Bulgarelli et al., 2025)

In conclusion, the modular approach of ARTEMIS-OC ensures effective and accurate in-house capabilities to model the radiance contributions received by OC satellite and *in situ* sensors, whether operating in oceanic, coastal, or inland waters.

1.1 The adjacency effects

Adjacency effects (AE) always occur in the presence of a scattering atmosphere over a non-uniform reflecting surface, which causes the radiance from high-reflectivity areas to spill over neighbouring low-reflectivity regions, thus modifying their apparent brightness (Otterman and Fraser, 1979). AE indeed describes the alteration in the apparent brightness of the observed surface element caused by atmospheric scattering of radiance originating outside the sensor element field of view.

Adjacency effects in satellite land observations have been comprehensively investigated for decades [see (Tanre et al., 1979; Kaufman, 1984, 1979; Pearce, 1986; Vermote and Vermeulen, 1999) and references therein], and related atmospheric correction codes routinely account for adjacency perturbations (e.g., Kaufman, 1984, 1979; Pearce, 1986; Vermote and Vermeulen, 1999).

On the contrary, most of the operational OC retrieval procedures still assume a uniform underlying water surface (Antoine and Morel, 1999; Gordon and Wang, 1994; Mobley et al., 2016). At present, only aquatic data acquired with the high-resolution Environmental Mapping and Analysis Program (EnMAP) (Storch et al., 2023) are operationally corrected for AE (Wenzel et al., 2022).

Nonetheless, OC products are susceptible to even small sources of noise (Hu et al., 2001), while the interpretation of the complex optical signal from coastal waters is challenged by the capability to properly account for the simultaneous presence of not-covarying in-water optically significant components [i.e., pigments, colored dissolved organic matter (CDOM), and suspended sediments], water bottom reflectance, and any AE induced by nearby mainland. As such, an accurate evaluation of the spectral perturbations induced by AE is needed to improve a correct interpretation of the signal from coastal and inland waters.

Until the last decade, studies on AE in coastal and inland waters were sparse (Reinersman and Carder, 1995; Yang and Gordon, 1997; Ruddick et al., 2000; Bélanger et al., 2007; Sterckx et al., 2011) and applied one or more simplifying assumptions, e.g., nadir observation (Sei, 2007), straight coastline (Sei, 2007), Lambertian reflecting surfaces (Sei, 2007; Reinersman and Carder, 1995), single scattering approximation (Santer and Schmechtig, 2000), and exponential decay of the environment effects (Sei, 2007; Santer and Schmechtig, 2000). Additionally, the uncertainties in simulated results were not explicitly discussed, and the radiometric sensitivity of the measuring sensors, which implicitly defines the threshold for discriminating adjacency effects from noise, was not explicitly taken into consideration.

Additional efforts have been recently dedicated to the analysis (Bulgarelli et al., 2018, 2017, 2014; Bulgarelli and Zibordi, 2020, 2018b, 2018a; Wu et al., 2023; Zhao et al., 2024) and the minimisation (Kiselev et al., 2015; Wu et al., 2024; Sei, 2015; Pan and Bélanger, 2024; Paulino et al., 2022) of AE.

Adjacency effects can be quantified in terms of the *adjacency radiance* L_{adj}, defined as the difference in the *background radiance* between the case accounting for the non-uniformity of the underlying reflecting surface and the case assuming a uniform surface. It is recalled that *i)* the *background radiance* (Deschamps et al., 1983) [also called *environmental radiance* (Sei, 2007)] identifies the radiance reflected by the background surface of the *target element* and then scattered by the atmosphere in the sensor instantaneous field-of-view (IFOV); and *ii)* the *target element* refers to the sensor effective footprint resulting from the intersection of the sensor IFOV with the ground for the whole sensor integration time (Robinson, 2004).

In agreement with (Bulgarelli et al., 2014), the adjacency radiance L_{adj} received by a space-sensor observing a sea-target element located in a coastal region at (x_0, y_0) with an observation direction $\boldsymbol{\xi}$ can be expressed as:

$$L_{adj}(x_0, y_0; \boldsymbol{\xi}) = \{\rho_l / [\pi(1 - \rho_l S)] - R_{rs}/(1 - \rho_{sea} S)\}\, C(x_0, y_0; \boldsymbol{\xi}) - W(x_0, y_0; \boldsymbol{\xi}) \tag{1}$$

In Eq 1, the unit vector $\boldsymbol{\xi}$ is defined as $\boldsymbol{\xi} = (\theta, \phi)$, where θ is the zenith angle measured from the nadir direction, and ϕ is the azimuth angle measured positive clockwise with respect to the north; term ρ_l indicates the albedo of the mainland assumed to be spatially homogeneous; ρ_{sea} represents the sea albedo, i.e., the albedo of both water and sea surface [pg. 193 of ref. (Mobley, 1994)]; S is the atmospheric spherical albedo of the bottom of the atmosphere; R_{rs} is the remote sensing reflectance; and:

$$C(x_0, y_0; \boldsymbol{\xi}) = E_d^{\rho=0}(x, y) \cdot M(x, y) \otimes h(x, y; x_0, y_0; \boldsymbol{\xi}', \boldsymbol{\xi}) \tag{2a}$$

and

$$W(x_0, y_0; \boldsymbol{\xi}) = L_{ss}(x, y; \boldsymbol{\xi}') \cdot M(x, y) \otimes h\,(x, y; x_0, y_0; \boldsymbol{\xi}', \boldsymbol{\xi}) \tag{2b}$$

In Eq. (2a) $E_d^{\rho=0}$ identifies the total downward irradiance at surface level for a completely absorbing surface; L_{ss} the radiance reflected by the sea surface; $h(x, y; x_0, y_0; \boldsymbol{\xi}', \boldsymbol{\xi})$ the atmospheric point-spread function (APSF), describing the transmission of the original signal through the propagating system; and $M(x, y)$ the land-water matrix:

$$M(x, y) = \begin{cases} 1 & \text{for land elements} \\ 0 & \text{otherwise} \end{cases} \tag{3}$$

The dependence on the sunbeam direction $\boldsymbol{\xi}_0$, the optical thickness τ, the single scattering albedo ω_0, the wavelength λ, and the scattering phase function has been omitted for simplicity.

Parameters ρ_l and R_{rs} can be extrapolated from satellite-derived and *in situ* measured data, respectively. Parameter ρ_{sea} appears in Eq. (1) only to account for multiple reflections at the sea surface, so it can be approximated without important loss in accuracy as

$$\rho_{sea} = \rho_{ss} + \rho_w \approx 0.04 + \pi R_{rs} \,, \tag{4}$$

where $\rho_{ss} \approx 0.04$ indicates a typical irradiance reflectance of the sea surface for the propagation from air to water [pg. 494 of ref. (Mobley, 1994)], while the water reflectance ρ_w simply equals πR_{rs} when assuming an isotropic angular distribution of the water-leaving radiance.

The simulation of term S can be performed with a plane-parallel radiative transfer code. The simulation of terms $C(x_0, y_0; \boldsymbol{\xi})$ and $W(x_0, y_0; \boldsymbol{\xi})$, instead, requires a full 3D description of the propagating system, and hence the use of a MC code.

The same methodology, developed for coastal regions, can be applied in inland water basins.

1.2 The RTE and the Monte Carlo method

A general overview of the radiative transfer equation (RTE) and of the Monte Carlo method is here provided.

The RTE describes the propagation of the radiance through a scattering, absorbing, and emitting medium. It is an integro-differential equation in the radiance L as a function of the position vector $\boldsymbol{r}$ of Cartesian coordinates and of the direction unit vector $\boldsymbol{\xi} = (\theta, \phi)$:

$$(\boldsymbol{\xi} \cdot \boldsymbol{\nabla})L(\boldsymbol{r}; \xi) = -c(\boldsymbol{r})L(\boldsymbol{r}; \boldsymbol{\xi}) + \int_{\Omega} L(\boldsymbol{r}; \boldsymbol{\xi}')\beta(\boldsymbol{r}; \boldsymbol{\xi}' \to \boldsymbol{\xi})d\Omega' + S(\boldsymbol{r}; \boldsymbol{\xi}) \tag{5}$$

In Eq. (5) $\boldsymbol{\nabla}$ represents the gradient operator; $c(\boldsymbol{r})$ the attenuation coefficient at $\boldsymbol{r}$; β is the volume scattering function (VSF) defining the probability that radiance at $\boldsymbol{r}$ from any direction $\boldsymbol{\xi}'$ is scattered into direction $\boldsymbol{\xi}$; and $S(\boldsymbol{r}; \boldsymbol{\xi})$ is the source term. The wavelength dependence has been omitted for brevity. It is reminded that $c(\boldsymbol{r}) = a(\boldsymbol{r}) + b(\boldsymbol{r})$, where $a(\boldsymbol{r})$ and $b(\boldsymbol{r}) = \int_{4\pi} \beta(\boldsymbol{r}; \boldsymbol{\xi}' \to \boldsymbol{\xi})d\Omega'$ denote the absorption and scattering coefficients, respectively.

Solving the RTE analytically is only feasible under very restrictive assumptions, making numerical methods (either deterministic or stochastic) the preferred approach in most cases.

Deterministic methods [e.g., the discrete-ordinate method (Liou, 2002; Mayer et al., 2011; Stamnes et al., 1988), the invariant imbedding technique (Mobley, 1994; Preisendorfer, 1976), the adding and doubling technique (Kneizys et al., 1988; Liou, 2002), the method of successive order of scattering (Gordon and Wang, 1992; van de Hulst, 1981) and the finite-elements method (Kisselev et al., 1995; Bulgarelli et al., 1999)] offer computational efficiency, but are characterised by mathematical intricacy and a lack of direct physical interpretation.

In contrast, the stochastic approach (i.e., that applied in the MC method) is mathematically simpler and physically direct, but results are inevitably affected by statistical uncertainties while the computing load is much heavier.

As a result, deterministic solutions are typically applied to solve the RTE in cases of horizontal translational invariance (i.e., in plane-parallel systems), while the MC method is preferred for more complex scenarios involving three-dimensional geometries and/or time-dependent processes.

Since the quantification of adjacency effects requires accounting for the non-uniformity of the underlying reflecting surface, the stochastic approach is the reference one.

The MC method solves the RTE by stochastically quantifying the percentage of virtual photons emitted by the source (initialised photons), which are detected by the radiometric sensor (D'Alimonte et al., 2010; Doyle and Rief, 1998; Prokhorov, 1998). The probability for the entire sequence of events is determined by the probability of each single event the photon may undergo in its "life history". In practice, the initialised photons are followed in their 3D path from the source to the sensor through the scattering and absorbing medium, using probability density functions p and cumulative distribution functions P to model all possible interactions.

The probability that an event *x* lies between *x* and (*x* + *dx*) is defined as $p(x)dx$ with:

$$\int_{-\infty}^{\infty} p(x)dx = 1; \tag{6}$$

while the probability for the same event *x* to lie between the lowest possible value x_{min} and *x* is defined as:

$$P(x) = \int_{x_{min}}^{x} p(x')dx' \tag{7}$$

with $0 \leq P(x) \leq 1$.

As so, by randomly selecting a number q uniformly distributed between 0 and 1, the solution of $P(x) = q$ allows statistically selecting *x* for each photon event.

For the specific case of radiance propagation in the atmosphere, probability functions are used to sample *i)* the optical distance (also called *optical depth*) $\tau = c \cdot d$ covered before interacting with the medium, (d is the geometrical distance to the next collision point); *ii)* the nature of the interaction event; *iii)* and the photon propagation direction after the event.

From the exponential decay of the probability density function of the optical distance, $p(\tau) = e^{-\tau}$, the free-flight optical distance τ is obtained as $\tau = -\ln q$.

The nature of each interaction with the medium is instead determined by comparing the sampled number q with the single-scattering albedo $\omega_0 = b/c$ (which defines the probability for an interaction to be a scattering event): if $q \leq \omega_0$, a scattering event occurs, otherwise the photon is absorbed.

The direction of the photon after each scattering event is finally determined through the scattering phase function $\tilde{\beta} = \beta/b$. Since adopted $\tilde{\beta}$ are azimuthally invariant and satisfy the normalisation condition $2\pi \int_0^{\pi} \tilde{\beta}(\theta) \sin(\theta)\, d\theta = 1$, the zenith angle θ is obtained from $P(\theta) \equiv 2\pi \int_0^{\theta} \tilde{\beta}(\theta') \sin(\theta')\, d\theta' = q$, while the azimuth angle is computed as $\phi = 2\pi q$.

In the interaction with the bottom boundary of the atmosphere, the direction of the reflected photon is determined via the bidirectional reflectance distribution function (BRDF [sr^{-1}]) of the reflecting surface. The BRDF defines the directional reflectance properties of the surface element, describing the reflection of a parallel beam of incident light from one direction into another direction in the same hemisphere (Kajiyama et al., 2016). In other words, it defines the probability that radiance impinging on the surface from a given direction $\boldsymbol{\xi}'$ is reflected into direction $\boldsymbol{\xi}$.

The accuracy of the MC simulation procedure depends on both a correct description of the propagating system, including its boundary conditions, and on the capability to constraint the random statistical noise, which is a linear function of the square root of the number of initialised photons N_{pho}.

Most MC methods apply variance-reducing techniques to inhibit photon loss, thus increasing computational efficiency and decreasing the statistical uncertainty.

A widely applied variance-reducing technique is the forced-collision sampling technique, which forces each interaction with the medium to be a scattering event, so that photons are not lost in absorption processes. This is achieved by associating a statistical photon weight w=1 at the source and by multiplying w by ω_0 at each photon interaction with the medium. The procedure is equivalent to consider a photon packet from which, at each event, absorbed photons are removed. The process is heuristically ended when w becomes smaller than a given threshold, so that photons are traced only as long as they appreciably contribute to model radiometric quantities. The threshold might be predefined [e.g., in the order of 10^{-6} (Kajiyama et al., 2016) or 10^{-7} (Bulgarelli et al., 2014)] or a function of the system Inherent Optical Properties (IOPs) and of the MC simulation accuracy requirements. Alternatively, the Russian Roulette technique can be applied (Iwabuchi, 2006).

Another extensively applied variance-reducing technique is the backward ray tracing: while in the forward MC method photons are started at the source and tracked to the detector, in the backward MC method, time reversal is applied, and photons are tracked from the detector back to the source. At each scattering event, the contributions to the detected signal are deterministically computed, ensuring highly increased computational efficiency.

Other variance-reducing techniques (not applied in NAUSICAA) include the phase function truncation technique to improve the handling of highly peaked scattering phase functions (Potter, 1970; Gordon, 1985; Hansen et al., 1969); the correlated sampling technique to allow simultaneously tracking the photon propagation in the presence and in the absence of the perturbing object (Spanier, 1969); and the semi-systematic sampling, which restricts the angular direction of the backward emitted or scattered photons to not yet sampled angular bins, allowing a more uniform selection of random directions (Lux et al., 1991).

2 The NAUSICAA code

2.1 Methodology

The NAUSICAA backward MC code simulates 3D optical photon transport in a inhomogeneous and physically realistic atmosphere bounded by a bottom non-uniform reflecting surface. The propagating medium is modeled on a 3D grid delimiting the macroscopic volumes or cells of uniform optical properties. The 3D grid is surrounded by a background plane-parallel atmosphere bounded by a bottom uniform reflecting surface.

For each cell of the grid, the characteristics of the optically active components (air molecules and aerosols) are specified through the extinction coefficient *c*, the single scattering albedo ω_0, and the scattering phase function $\tilde{\beta}$. A Rayleigh phase function is assumed for the gas molecules. The aerosol scattering phase function $\tilde{\beta}_{aer}$ can be either modeled as a two-term Henyey–Greenstein (TTHG) phase function (Henyey and Greenstein, 1941; Kattawar, 1975) or provided in a tabulated form. In the first case, the angular distribution function $P(\theta)$ (see eq. 7) is also expressed in analytical terms.

Each element of the bottom reflecting surface can be characterised either by a Fresnel specular reflectance (suitable for a flat water-surface) or by the surface BRDF. The accurate expression of the BRDF for a wind-generated rough water-surface is taken from (Kisselev and Bulgarelli, 2004). This is preferred to the well-known BRDF expression from (Cox and Munk, 1954) because, although based on the same two-dimensional Gaussian water-surface wave slope distribution (Cox and Munk, 1954), it does not tend to infinity for reflections close to the horizontal direction.

The approach to model the reflectance of a wind-roughed water surface through the BRDF is applied to ensure an equivalent sampling of photons interacting with the land and photons interacting with the water surface, thus avoiding the eventual occurrence of artificial biases induced by oversampling one type of photons with respect to the other. The presence of whitecaps is not accounted for. The latter assumption is reasonable for wind speeds lower than about 7 ms^{-1} (Monahan and O'Muircheartaigh, 1986).

The parametric semi-empirical model developed by (Rahman et al., 1993), the so-called RPV, is implemented to obtain realistic land BRDF (Pinty et al., 2002). The overall shape of the angular distribution is defined through three parameters: ρ_0, representing the reflectance of the surface for illumination and viewing at the zenith; *k*, controlling the slope of the reflectance with respect to illumination and viewing angles [close to 1.0 for a quasi-Lambertian surface, lower (higher) than 1.0 when a bowl-shaped (bell-shaped) pattern dominates]; and Θ that establishes the degree of forward (positive Θ) or backward (negative Θ) scattering.

The solar source is described by a parallel beam of monochromatic photons that originates from a far-field point and uniformly impinges on the top of atmosphere (TOA).

For any given target surface-element, the backward MC code releases photons from the satellite sensor in the observation direction and with initial unitary statistical weight. The time-reversal scheme is applied to track photons from the detector back to the source. At first, the optical distance to the first collision point is sampled. The distance to collision is recomputed when the photon crosses a cell boundary before interacting with the medium, and the photon is re-launched from the boundary itself. At the collision point, a scattering event is forced by multiplying the photon weight w by ω_0. The type of scattering (either by molecules or aerosols) is sampled, and a new propagation direction of the surviving photon is determined by retrieving the scattering angle from random sampling of the distribution function $P(\theta)$. Upon sampling a new distance to the collision point, the photon is re-launched.

If the photon reaches a specular surface element, a reflection is forced by multiplying the photon weight by the Fresnel reflection coefficient, and the new direction of the photon is deterministically calculated. Otherwise, if the surface element is not specular, the photon weight is multiplied by the directional–hemispherical reflectance [DHR, i.e., the reflectance for incoming light from a single direction (Martonchik et al., 2000)] at the point of reflection, and the photon interaction with the surface is treated as in a collision event.

The distance to the next collision point is sampled again, and the whole process is repeated until the statistical weight of the tracked photon falls below a preset threshold value. Alternatively, the survival of the photon packet is determined randomly through the Russian roulette method (Iwabuchi, 2006).

At any collision, the contribution of the tracked photons to the detected signal is deterministically computed. In the presence of flat water-surface areas, the eventual contribution of the direct solar beam specularly reflected by the water surface is accounted for.

For the simulation of functions *C* and *W* (see Eq. 2), only the contributions from photons that already interacted with the underlying reflecting surface are retained. Additionally, water surface elements are assumed totally absorbing, while land elements are modeled with land BRDF in the simulation of function *C*, and with a uniform wind-generated rough water-surface BRDF for the simulation of function *W.*

Simulated results are provided with their statistical uncertainty, as determined by the selected number of initiated photons N_{pho} and by the threshold for photon survival (Roberti, 1997).

2.2 Atmospheric Modeling

The code can ingest any atmospheric description produced by the PERSEA code (Bulgarelli and Vitale, in progress).

2.3 Inputs and outputs

Inputs required by the main subroutine (*NAUSICAA_RTE_solver.f*) are here described. Additional details are provided in Annex 1.

2.3.1 Medium structure

The size of the cells in which the medium is gridded can vary both vertically and horizontally (Fig. 7). In specific, the medium is modelled by *NXCL* x *NYCL* horizontally finite and vertically layered columns, with a square base of dimension *SIZE* (in km); both the height (*LYRHGT*) and the number of the layers (*NLYR*) can vary from column to column, only the height of the top layer must be the same. The background plane-parallel atmosphere bounded by a bottom uniform reflecting surfaces is identified by coordinates $(0,0)$.

Figure 7. Scheme for medium structure. The background has coordinates (0,0)

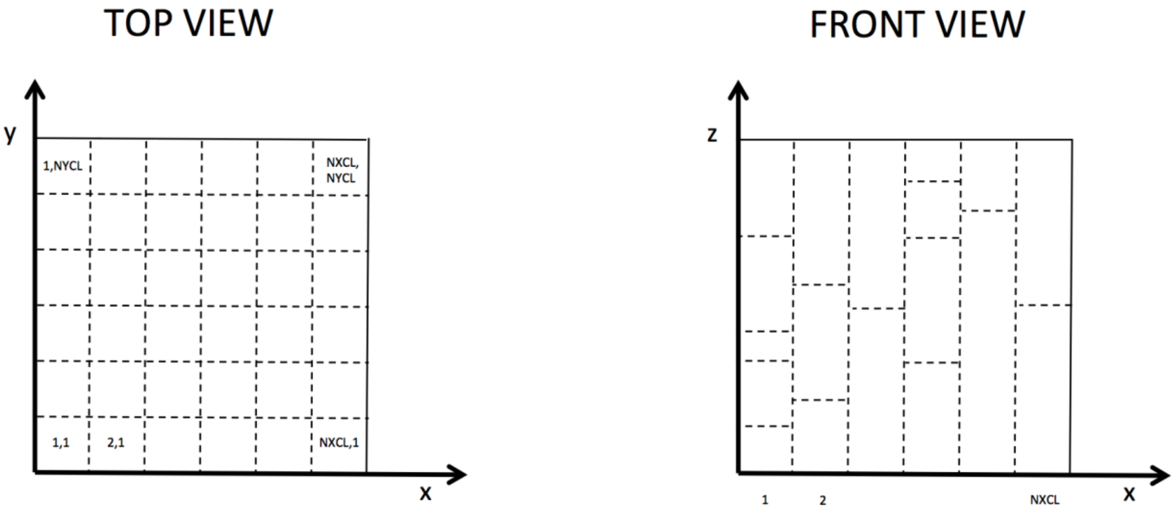

Source: Bulgarelli et al., 2025

2.3.2 Cells optical properties

The optical properties within each cell are assumed homogeneous. If a number N_c of optically active components is present, the global optical properties of each cell are:

- global extinction coefficient $c = \sum_{i=1}^{N_c} c_i$; notably the optical thickness is defined as $\tau = \int_{z_{bottom}}^{z_{top}} c \cdot dz$
- global single scattering albedo $\omega_0 = \frac{\sum_{i=1}^{N_c} \omega_{0i}\tau_i}{\sum_{i=1}^{N_c} \tau_i}$
- probability that the scattering event is due to aerosol $P_{aer}^{sc} = \frac{\omega_{0aer}\tau_{aer}}{\sum_{i=1}^{N_c} \omega_{0i}\tau_i}$
- aerosol phase function $\tilde{\beta}_{aer}$. Phase functions $\tilde{\beta}(\cos\Theta)$, where Θ is the scattering angle, are assumed symmetric in the azimuthal direction and are normalised to 1, i.e., $\int_{-1}^{1} \tilde{\beta}(\cos\Theta) d\cos\Theta = 1$. When flag *HENYEY* is set to *.true.*, $\tilde{\beta}_{aer}$ is modelled as a TTHG with parameters g_1, g_2, as; alternatively, $\tilde{\beta}_{aer}$ is read from the *FILEPHA* input file, where it must be provided tabulated by points.

2.3.3 Surface optical properties

Each square element of the surface (i.e., the lower boundary of the grid system) can either be characterised by

- a Lambertian land cover (flag *LAMBERT* must be set to *.true.* and the albedo *ALBE* must be provided in the range 0 to 1) or
- by a wind-roughened water surface (flag *LAMBERT* must be set to *.false.* and *ALBE* must be set to 99.9). In the latter case, the BRDF for a wind-generated rough water-surface is taken either from (Cox and Munk, 1954) or from (Kisselev and Bulgarelli, 2004).

The albedo of the background is identified as *ALBE(0,0)*; an example of surface grid is provided in Fig. 8.

It is noted that the subroutine also includes the possibility to select a BRDF according to (Pinty et al., 2005) for land surface elements (not operationally implemented).

Figure 8. Example of the surface grid. The background surface has coordinates (0,0)

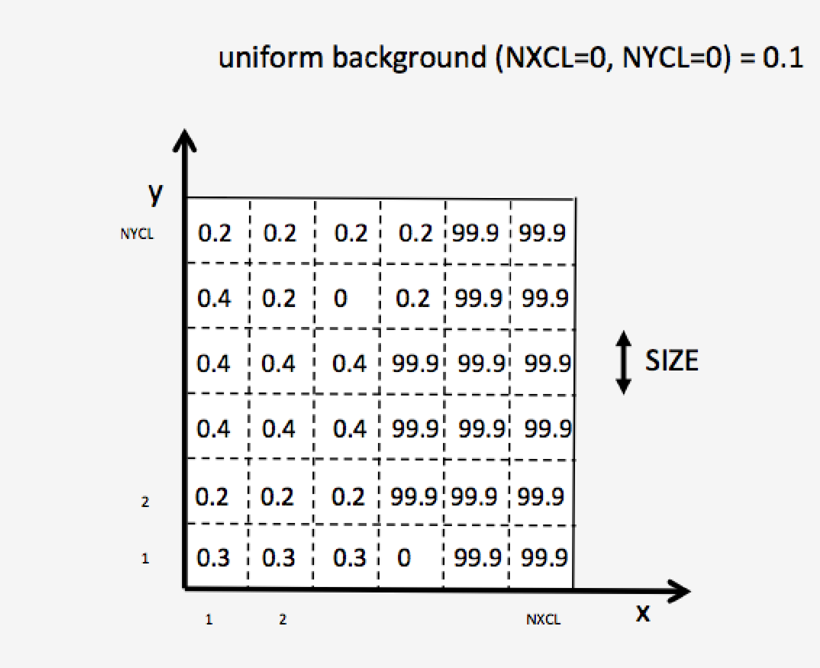

0.2	0.2	0.2	0.2	99.9	99.9
0.4	0.2	0	0.2	99.9	99.9
0.4	0.4	0.4	99.9	99.9	99.9
0.4	0.4	0.4	99.9	99.9	99.9
0.2	0.2	0.2	99.9	99.9	99.9
0.3	0.3	0.3	0	99.9	99.9

Source: Bulgarelli et al., 2025

2.3.4 Illumination conditions

The incident radiation is a parallel flux of irradiance F_0 impinging on the top boundary.

The illumination geometry, which identifies the direction of the incident sunbeam, is specified through

- the cosine of the sunbeam zenith angle $\theta_{sunbeam}$. It equals -1.0 when the sun is at nadir.
- the sunbeam azimuthal angle $\phi_{sunbeam}$ (in degrees), measured anticlockwise from the x-axis.

Fig. 9 shows that, given the sun angles θ_0 (with respect to zenith) and φ_0 (anticlockwise from the x-axis): $cos\theta_{sunbeam} = -cos\theta_0$; $\phi_{sunbeam} = \phi_0 + 180^o$ for $\phi_{sunbeam} < 180^o$, and $\phi_0 - 180^o$ for $\phi_{sunbeam} > 180^o$.

Figure 9. Scheme of the sunbeam geometry

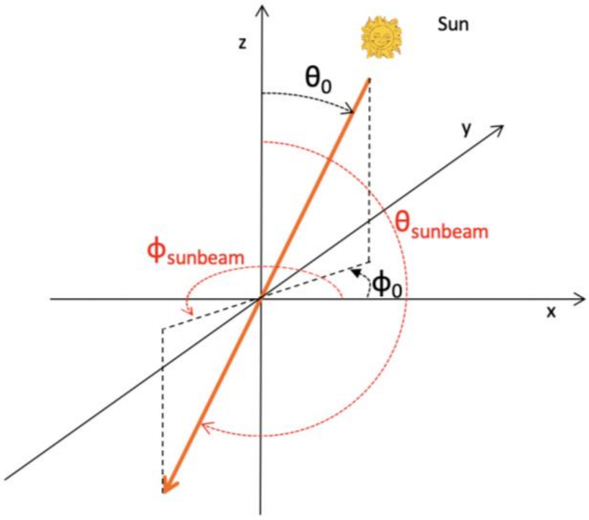

Source: Bulgarelli et al., 2025

2.3.5 Output geometry

NAUSICAA can compute the output radiance in any given position and direction.

The computational position of the output radiance is identified by the cartesian coordinates *POSX, POSY* and *POSZ* [km]; its computational direction is defined by the azimuth angle ϕ (in degree) measured anticlockwise from the x-axis, and the cosine of the zenith angle θ, measured with respect to the z-axis. Notably, positive cosines denote the upwelling radiance, negative ones the downwelling radiance, and $\cos\theta = 1$ corresponds to radiance propagating towards nadir.

For a satellite sensor, whose viewing geometry is identified by coordinates θ_v with respect to nadir and ϕ_v anticlockwise with respect to the x-axis, it simply is $\theta = \theta_v$, and $\phi = \phi_v$ (see Fig. 10).

Figure 10. Scheme of the output radiance geometry

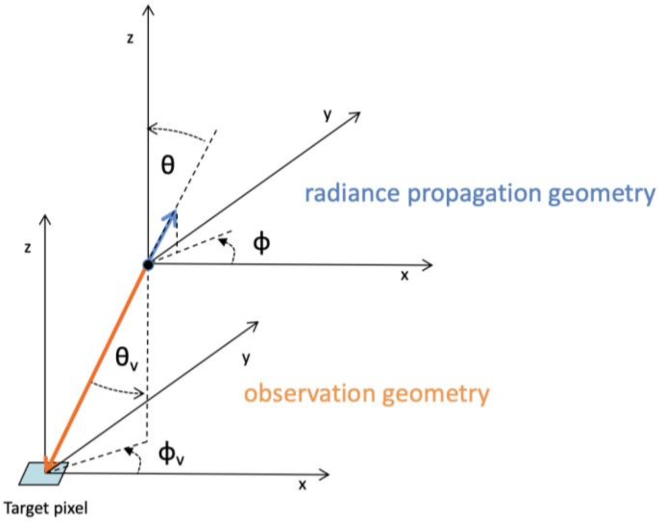

Source: Bulgarelli et al., 2025

2.3.6 Number of photons and output radiance

A number N_{pho} of photons is started at the sensor in the backward direction, and the total radiance detected by the sensor is computed as

$$L = \sum_{n}^{1,\mathrm{N_{pho}}} L_n \tag{8}$$

where L_n is the radiance associated with the *n*-th photon.

3 NAUSICAA accuracy and validation

The uncertainty $\sigma_{L_{adj}}^{MC}$ on the simulated adjacency radiance L_{adj} (see Eq. 1) can be expressed as:

$$\sigma_{L_{adj}}^{MC} = \left[\left(\sigma_{L_{adj}}^{rnd}\right)^2 + \left(\delta_{L_{adj}}^{sys}\right)^2\right]^{1/2}, \tag{9}$$

where $\sigma_{L_{adj}}^{rnd}$ and $\delta_{L_{adj}}^{sys}$ denote the contribution from *random* and *systematic* uncertainties of MC computations, respectively. Notably, random uncertainties inherently affect MC computations and strictly depend on the number of initialised photons N_{pho} and on the selected threshold for photon survival.

Contributions from statistical uncertainties $\sigma_{L_{adj}}^{rnd}$ may be required to be below a certain threshold.

As an example, in (Bulgarelli et al., 2014) $\sigma_{L_{adj}}^{rnd}$ in NAUSICAA simulations was required to be lower than the average OC sensors *Noise Equivalent Radiance Difference* $\overline{NE\Delta L} = 2F_0 \times 10^{-5}$ Wm^2 µm^{-1} sr^{-1}. $NE\Delta L$ represents the at-sensor incremental radiance that can still be discriminated from noise when observing a typical signal, and thus characterising the radiometric resolution of the sensor. Notably, by initialising $N_{pho} = 10^7$ photons, the requirement was fully satisfied.

In the same study (Bulgarelli et al., 2014) the contributions due to systematic uncertainties (biases) affecting the NAUSICAA computations, $\delta_{L_{adj}}^{sys}$, were evaluated by comparing upwelling surface radiances at TOA obtained for an infinite uniform reflecting surface with the corresponding values from the totally converged solution of the highly accurate FEM numerical code (Bulgarelli et al., 1999; Kisselev et al., 1995; Bulgarelli, 2024), assumed as the reference. The analysis, performed for several representative and realistic test cases by initialising $N_{pho} = 10^7$ photons and assuming *i)* an ideal (lossless) perfectly diffuse (Lambertian) surface and *ii)* a Fresnel-reflecting surface, indicated the absence of biases between FEM and NAUSICAA results (see Fig. 11). The optimal agreement between the two codes, which implement entirely different approaches to solve the RTE, provided a robust validation for the NAUSICAA algorithm. Moreover, biases never exceeded the statistical uncertainty of MC simulations with a 99.7% level of confidence.

NAUSICAA simulated results were further benchmarked with data obtained from the literature, showing optimal agreement (Bulgarelli et al., 2014).

Figure 11. Normalised distributions of $\delta_{MC\text{-}FEM}/E_0=(L_{sfcMC}^{TOA}– L_{sfcFEM}^{TOA})/E_0$ [sr^{-1}] for 672 test cases (N_{cases}) obtained by initialising $N_{pho}=10^7$ photons and assuming (a) a uniform ideal Lambertian surface and (b) a uniform Fresnel-reflecting surface. The Gaussian fit of the distributions is displayed in black. Its mean $<\delta/E_0>$ and standard deviation σ_δ/E_0 are also given. Note that the *x*-scale for the Lambertian case is one order of magnitude higher than that of the Fresnel case. L_{sfc}^{TOA} indicates the upwelling surface radiance at TOA.

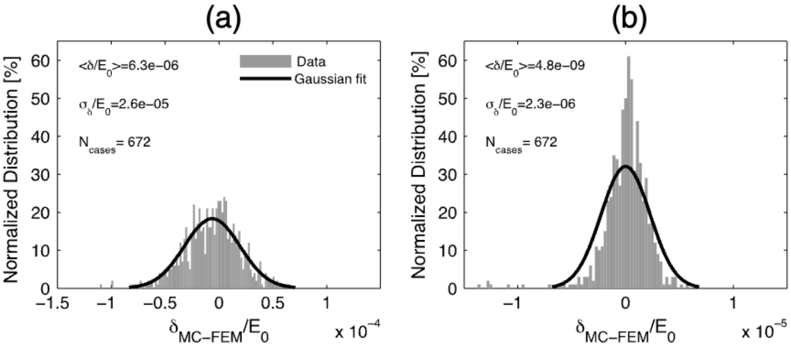

Source: (Bulgarelli et al., 2014)

4 NAUSICAA computational efficiency

The MC transport of each photon at the core of NAUSICAA simulations is independent of the other photons, and their order is not relevant, which means that RT simulations distributed over multiple computing units are statistically equivalent to those obtained with a single one. Parallel execution over different computing units was then adopted to reduce the actual simulation time.

Solutions to enhance the NAUSICAA efficiency are presented in this section.

4.1 Implementation framework

The NAUSICAA computational efficiency is optimised through the parallelisation of

- the innermost loop over each member of the photons' population, and
- the outer nested loops over a two-dimensional (2D) grid of pixels along the *x* and *y* axes.

The innermost loop optimisation divides the total number of photons N_{pho} into subsets, hence requiring limited code adaptations for parallel runs. Memory payload optimisation is additionally applied to enhance efficiency.

The nested loops over two spatial dimensions are transformed into a unified loop to facilitate parallelisation upon masking out-of-scope pixels (see Fig. 12). A fine-blocking approach is then adopted to balance the workload among the computing units.

Figure 12. Schematic of NAUSICAA steps for parallel computing through a) pixels masking, b) workload balancing, and c) distributed processing.

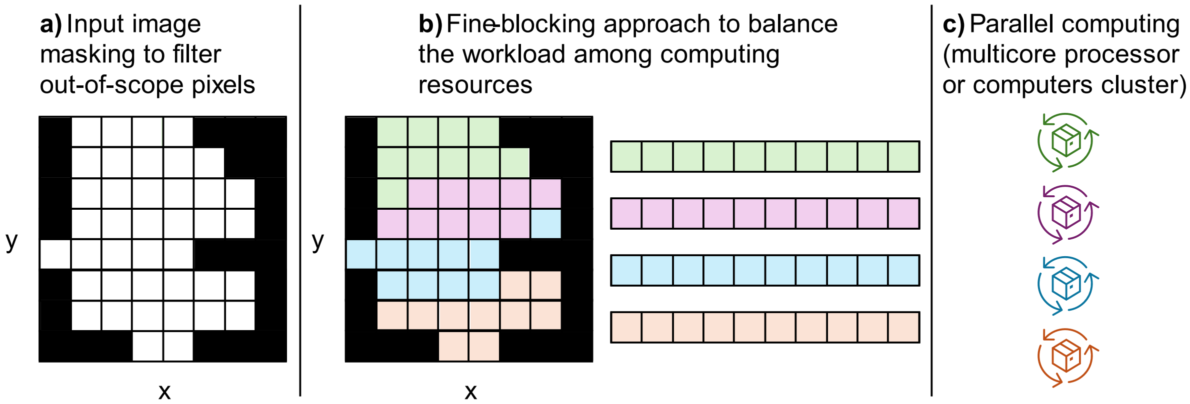

Source: (Bulgarelli et al., 2025)

The optimisation over the inner loop (i.e., over photons) or the outer loop (i.e., over space), which are mutually exclusive, is selected based on application requirements.

Two different versions of the NAUSICAA code have been implemented for parallel computing, one on a single multicore machine using the OpenMP toolset, and the other on a computer cluster using the Message Passing Interface (MPI) toolset, see Fig. 13, panels a) and b), respectively.

Figure 13. Schematic of NAUSICAA simulations on a) multicore machine and b) computer cluster.

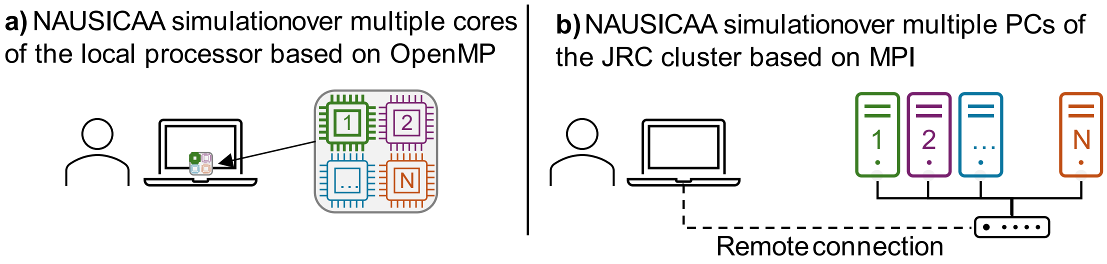

Source: (Bulgarelli et al., 2025)

Although the code parallelisation and the tasks assignment to different computing units are intuitive, actual implementations imply careful adaptation of the original sequential code.

Among those addressed for NAUSICAA is the random number generation underpinning MC photon transport. Precisely, *i)* the *RAND* and *SRAND* intrinsic functions used in the original sequential NAUSICAA code were assessed as unapplicable for distributed processing because the random number generator state may corrupt due to uncoordinated simultaneous updates by multiple threads of execution, i.e., a phenomenon referred to as “not thread-safe”; and *ii)* multiple computing units may share the same random number seed. These pitfalls have been sorted out as follows. First, the thread-safe *RANDOM_NUMBER* and *RANDOM_SEED* subroutines are used instead of *RAND* and *SRAND*, respectively. Second, unique random number seeds are instantiated by individual computing units, each based on a specific identifier. Numerical tests confirmed that there is no correlation between random number sequences.

4.2 Performance assessments

The NAUSICAA performance efficiency is documented through illustrative test cases.

Optimisation for speed by parallelised loops is evaluated through the execution time *T* as a function of the number of computing units (i.e., either threads in OpenMP or processes in MPI). Additional performance metrics are speedup η and parallel efficiency ε.

The speedup η is defined as:

$$\eta(N) = \frac{T(1)}{T(N)} \quad , \tag{10}$$

where $T(1)$ is the execution time in the case of a single computing unit used as a benchmark, and $T(N)$ is that resulting from N computing units. The aimed result is $T(N) < T(1)$—i.e., the processing time is reduced by distributing parallel tasks over computing units—and hence, the larger η, the better.

The parallel efficiency ε is defined as:

$$\varepsilon(N) = 100 \cdot \frac{T(1)}{N \cdot T(N)} = 100 \cdot \frac{\eta(N)}{N} \quad . \tag{11}$$

The best efficiency occurs when the processing time scales as the number of computing units (e.g., if $N = 2$ and $T(2) = T(1)/2$, then in this case $\varepsilon = 100\%$). In practice, $\varepsilon < 100\%$ because parallel processing requires supplemental operations, such as sharing initialisations and gathering results, besides photon tracing. The more demanding these supplemental operations w.r.t. the actual MC tracing, the lower the efficiency. Note that the efficiency also varies between OpenMP and MPI because of different underlying parallel operation requirements.

Results about the parallelisations of the loop over photons and that over observational pixels are presented below to illustrate how concurring factors drive the efficiency of the NAUSICAA code. Performance tests are generated with a number of computing units (either OpenMP threads or MPI processes) ranging from 2 to 12.

4.2.1 **Parallelised loop over photons**

Performance figures presented in Figs. 14 and 15 are also detailed in Table 1. Results indicate that an increased number of photons leads to better speedups and efficiency rates because of relatively fewer parallelisation overheads. Examples are the time spent on *i)* the creation and finalisation of OpenMP threads and *ii)* data transfers among MPI processes. In the present performance tests, the best $\eta = 4.07$ is obtained with the MPI-parallel version when 10^6 photons were traced using 12 processes.

Performance results for computer clusters using MPI show the efficiency η lowering for N_{cmp} from 8 to 12, likely due to frequent data transfers within the parallelised loop over pixels, where collective data communications (by the *MPI_Gather* subroutine) are performed among MPI processes for each loop iteration. Increasing the number of photons lessens the relative weight of data communication w.r.t photon tracing.

Figure 14. Performance of the OpenMP-parallel version of the NAUSICAA code featuring the parallelised loop over photons.

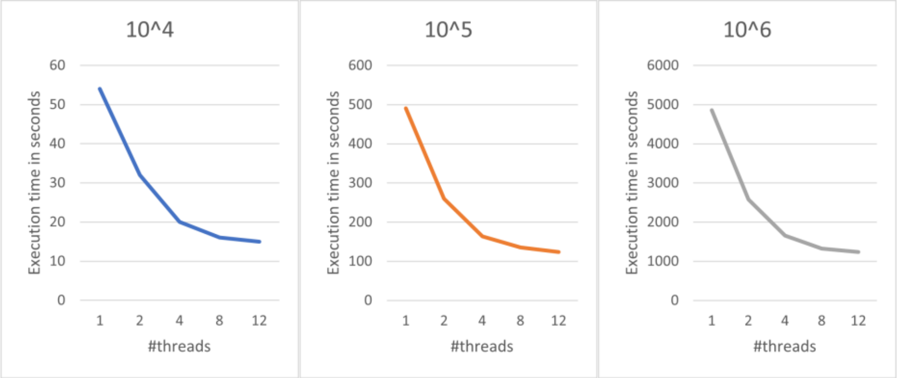

Source: (Bulgarelli et al., 2025)

Figure 15. Performance of the MPI-parallel version of the NAUSICAA code featuring the parallelised loop over photons.

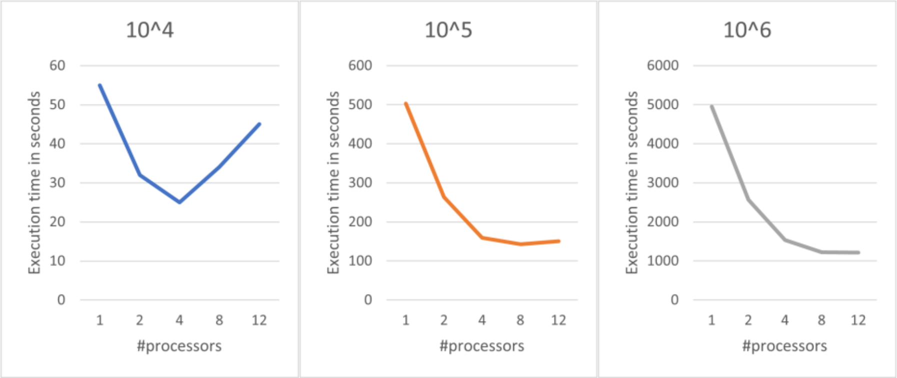

Source: (Bulgarelli et al., 2025)

Table 1 Performance results of the NAUSICAA code with the parallelised loop over photons for a multicore machines using OpenMP and for a computer clusters based on MPI.

		Multicore machine (Open MP)			Computer cluster (MPI)		
N_{pho}	N_{cmp}	T [sec.]	η	ε	T [sec.]	η	ε
10^4	1	54	N/A	N/A	55	N/A	N/A
	2	32	1.69	84%	32	1.72	86%
	4	20	2.70	68%	25	2.20	55%
	8	16	3.38	42%	34	1.62	20%
	12	15	3.60	30%	45	1.22	10%
10^5	1	491	N/A	N/A	503	N/A	N/A
	2	260	1.89	94%	263	1.91	96%
	4	164	2.99	75%	159	3.16	79%
	8	135	3.64	45%	143	3.52	44%
	12	124	3.96	33%	151	3.33	28%
10^6	1	4,856	N/A	N/A	4,952	N/A	N/A
	2	2,579	1.88	94%	2,563	1.93	97%
	4	1,650	2.94	74%	1,539	3.22	80%
	8	1,326	3.66	46%	1,227	4.04	50%
	12	1,235	3.93	33%	1,216	4.07	34%

Source: (Bulgarelli et al., 2025)

4.2.2 Parallelised loop over observational pixels

Performance results considering the parallel loop over pixels are visualised in Figs. 16 and 17 and shown in Table 2. The OpenMP-based parallel loop over pixels resulted in better η and ε values when compared with the OpenMP-based parallel loop over photons (see Table 1), likely due to a coarser division of workload (i.e., pixels instead of photons) and hence fewer parallelisation overheads. The best speedup $\eta = 8.45$ is obtained using 12 OpenMP threads.

Figure 16. Performance of the OpenMP-parallel version of the NAUSICAA code featuring the parallelised loop over masked observational pixels.

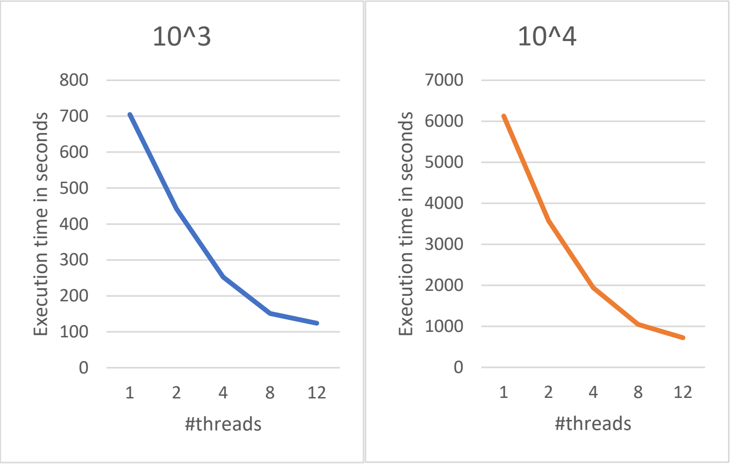

Source: (Bulgarelli et al., 2025)

Figure 17. Performance of the MPI-parallel version of the NAUSICAA code featuring the parallelised loop over masked observational pixels.

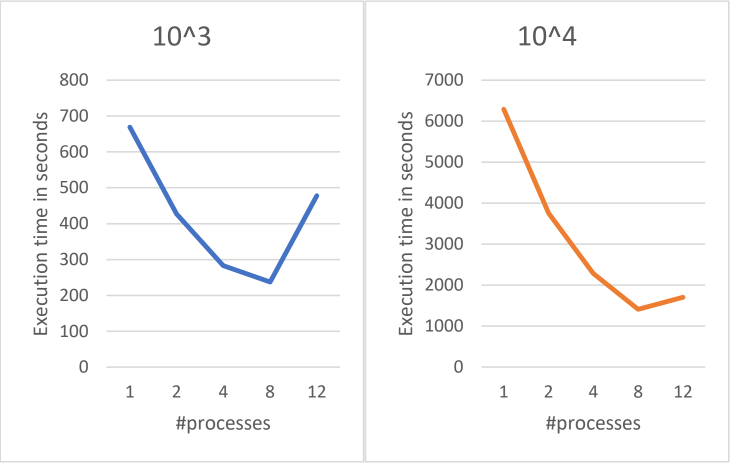

Source: (Bulgarelli et al., 2025)

Table 2 Performance results of the NAUSICAA code with the parallelised loop over masked observational pixels for a multicore machine using OpenMP and a computer cluster based on MPI.

		Multicore machine (OpenMP)			Computer cluster (MPI)		
N_{pho}	N_{cmp}	T [sec.]	η	ε	T [sec.]	η	ε
10^3	1	705	N/A	N/A	669	N/A	N/A
	2	442	1.60	80%	427	1.57	78%
	4	252	2.80	70%	283	2.36	59%
	8	151	4.67	58%	237	2.82	35%
	12	124	5.69	47%	478	1.40	12%
10^4	1	6,129	N/A	N/A	6,286	N/A	N/A
	2	3,572	1.72	86%	3,750	1.68	84%
	4	1,942	3.16	79%	2,285	2.75	69%
	8	1,046	5.86	73%	1,409	4.46	56%
	12	725	8.45	70%	1,704	3.69	31%

Source: (Bulgarelli et al., 2025)

5 NAUSICAA code applications

This section presents main applications of the NAUSICAA code, additional details can be found in the published studies.

5.1 JRC analysis of adjacency effects in satellite data and satellite data products at a coastal validation site

The NAUSICAA code was extensively applied (Bulgarelli et al., 2014, 2018; Bulgarelli and Zibordi, 2018b; to investigate AE in OC satellite data and data products at the Aqua Alta Oceanographic Tower (AAOT, 45.31° N, 12.51° E; see Fig. 18): a validation site located in the northern Adriatic Sea at 8 nautical miles from the coast and belonging to the Ocean Color component of the Aerosol Robotic Network (AERONET-OC) (Zibordi et al., 2021, 2010, 2009).

The AAOT site was selected for two main reasons. Since 1995, the site has been used to validate satellite OC products (Zibordi et al., 2002) and its comprehensive multiannual record of in situ measurements (Zibordi et al., 2002, 2009, 2024) allows a precise definition of realistic and seasonally dependent test cases for the analysis of the adjacency effects. Additionally, the region hosting the AAOT is well representative of mid-latitude coastal areas covered by a deciduous vegetation type (the most diffuse in Europe) in the absence of snow, while the AAOT aerosol optical properties correspond to those mostly encountered at different AERONET-OC sites (Mélin et al., 2013). The analysis of AE at the site can thus provide insights into a variety of measurement conditions and coastal regions.

The study, performed for realistic and representative observation conditions, accounted for sea surface reflectance anisotropy, off-nadir views, coastal morphology, and atmospheric multiple scattering.

Results, computed along a transect encompassing the AAOT site (Fig. 18), highlight that, within the accuracy limits defined by the radiometric resolution of OC sensors, AE in coastal waters might be significant at both visible and near-infrared wavelengths up to several kilometres off the coast. Results additionally show a noteworthy dependence on the angle of observation, on the directional reflectance properties of the water surface, and on the atmospheric multiple scattering. Adjacency effects further exhibit a strong seasonal dependence, with increased values in summer when the land is highly reflecting, the water is highly absorbing, and the sun elevation is high. The impact of common approximations, like isotropic reflecting surface, nadir-observation geometry, single scattering approximation and straight coastline were also investigated.

Exemplificative results are given in Fig. 19 and 20.

Fig. 19 shows average simulated values of the percentage adjacency effects ($\xi_{L_{tot}} = L_{adj}/L_{tot} \cdot 100$) computed along the study transect of Fig. 18 at representative center-wavelengths.

Fig. 20 illustrates the impact of adjacency effects at the AAOT accounting for the noise level NL (equivalent to the inverse of the sensor-noise-ratio SNR) of reference OC sensors (namely, NASA SeaWiFS and MODIS, Landsat OLI, ESA MERIS, Sentinel-2 MSI and Sentinel-3 OLCI). Notably, sensors' NL were normalised to the same typical input radiance L_{typ} (Bulgarelli and Zibordi, 2018b; Hu et al., 2012).

Figure 18. (a) Region considered in NAUSICAA simulations (AAOT as a black circle, 45.31° N, 12.51° E). (b) Land/water mask: land elements are indicated in dark grey, and water elements are in light grey. The black line represents the transect intersecting the AAOT.

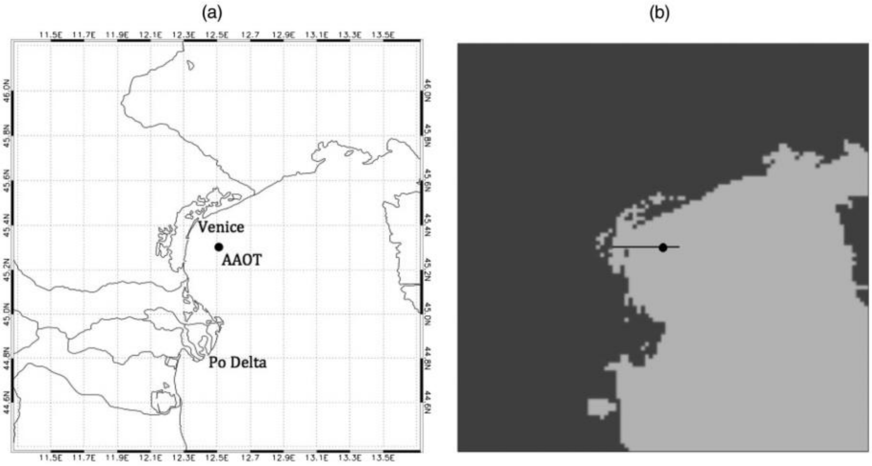

Source: (Bulgarelli et al., 2014)

Figure 19. Values of mean ξ_{Ltot} at representative wavelengths along the study transect. Error bars represent the standard deviation σ (black) and the sample variance (gray). L_w is assumed constant along the transect. The vertical dotted line identifies the position of the AAOT site.

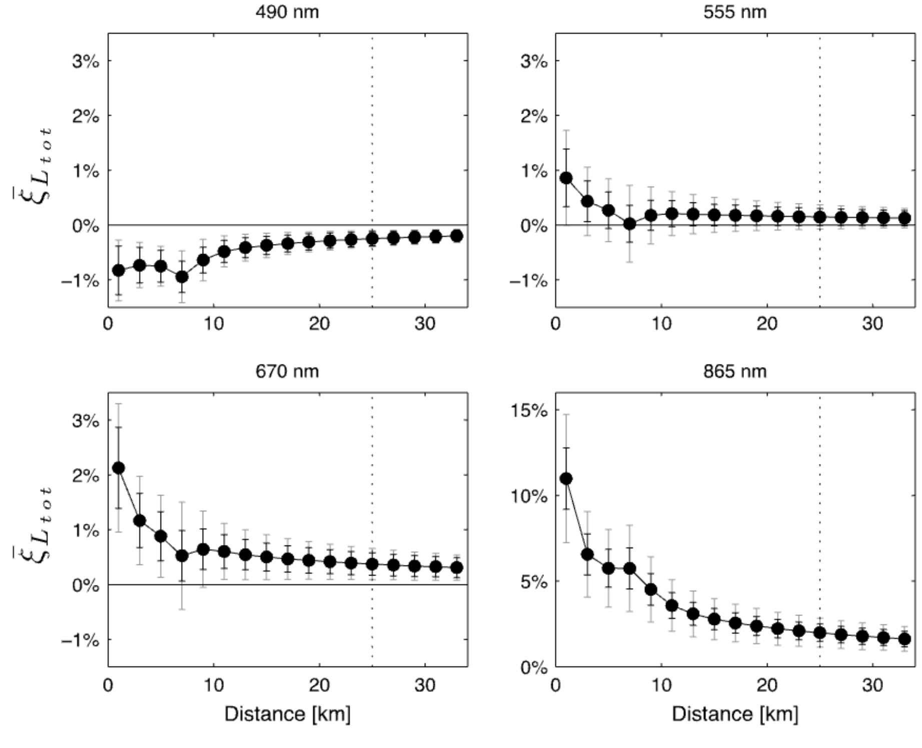

Source: (Bulgarelli et al., 2014)

Figure 20. Spectral annual average values of L_{adj} [$Wm^{-2}\mu m^{-1}sr^{-1}$] at SeaWiFS-equivalent centre-wavelengths for reference OC sensors. Black errorbars represent uncertainties for uncorrelated contributions; grey error bars indicate ±1 standard deviation (number of test cases N = 6 for OLI, 12 for MSI, 18 for the other sensors). Shaded and empty box bars indicate one and two harmonised sensor spectral NEΔL, respectively. LR=low resolution; HR: high resolution; FR=full resolution; RR=reduced resolution.

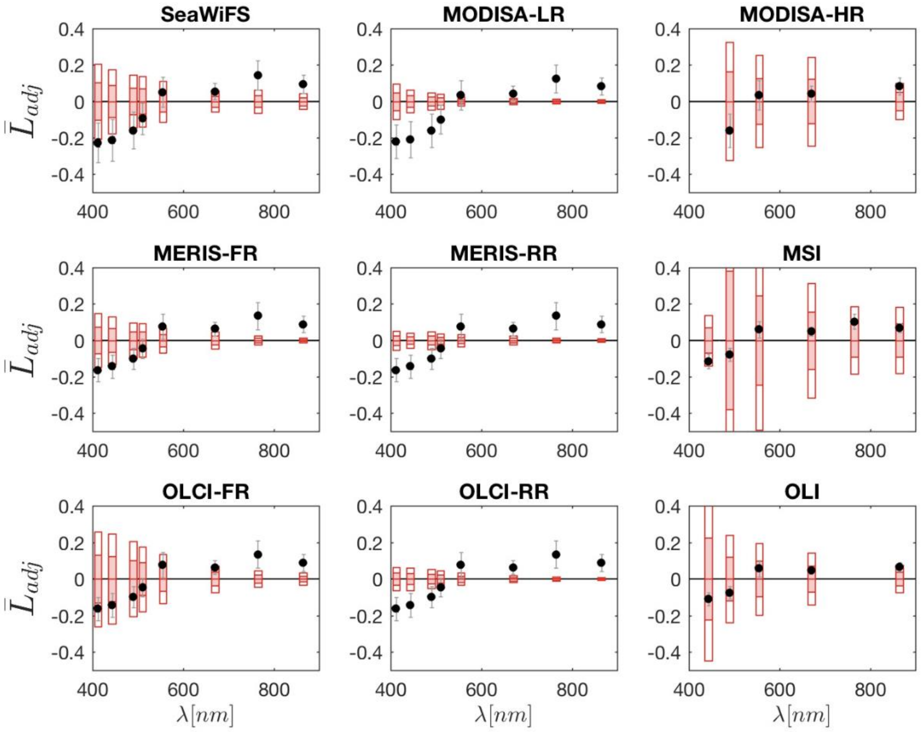

Source: (Bulgarelli and Zibordi, 2018b)

AE perturbations in satellite radiometric products strictly depend on the atmospheric correction (AC) procedure. To acknowledge this, biases ψ_{tL_w} on the retrieved water-leaving radiance at TOA, tL_w, were analysed for two different AC procedures: not deriving (AC-1) or deriving (AC-2) the atmospheric properties from the remote sensing data (Bulgarelli et al., 2017). Results along the study transect are depicted in Figs. 21 and 22, respectively.

For an AC-1 scheme, average biases ψ_{tL_w} are negligible throughout the study transect at yellow-green wavelengths, while they reach up to −21% and +34% at the coast at 412 and 670 nm, respectively (Fig. 21).

For the specific case of an AC-2 scheme determining the atmospheric properties from the NIR and by adopting a power-law spectral extrapolation of adjacency perturbations on the derived atmospheric radiance, average biases ψ_{tL_w} become all negative with values well exceeding −50% at 412 and 670 nm at the coast (Fig.22).

Figure 21. Annual average biases ψ_{tLw} at representative wavelengths for an AC-1 scheme. Results are presented as a function of the distance along the study transect (see Fig. 18), and error bars indicate the standard deviation ± σ_ψ (black, not visible in the present plots) and the sample variance (grey). L_w is assumed constant all along the transect. The horizontal dotted lines indicate ± 5%, while the vertical dashed line identifies the position of the AAOT site.

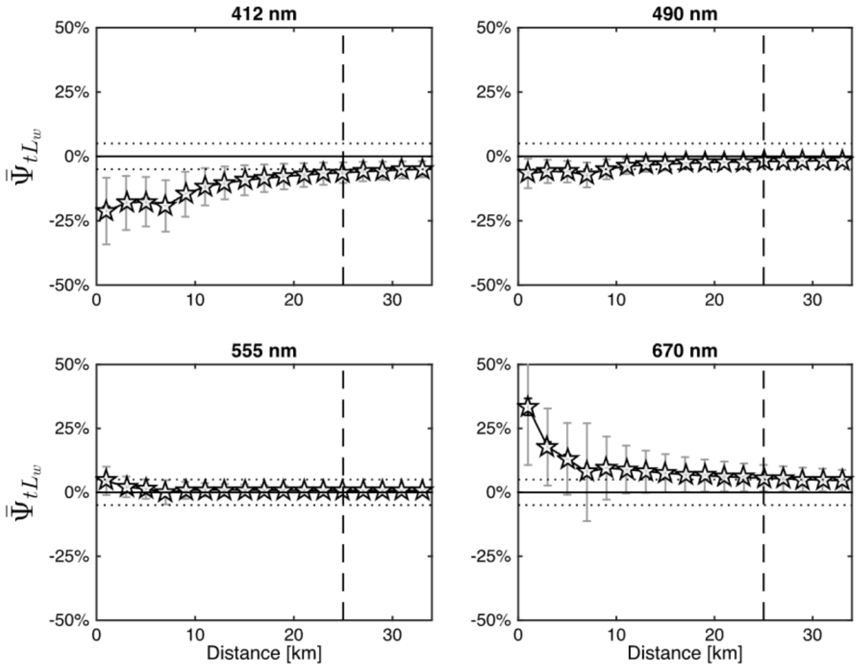

Source: (Bulgarelli et al., 2017)

Figure 22. As in Fig. 21 but for the AC-2 scheme

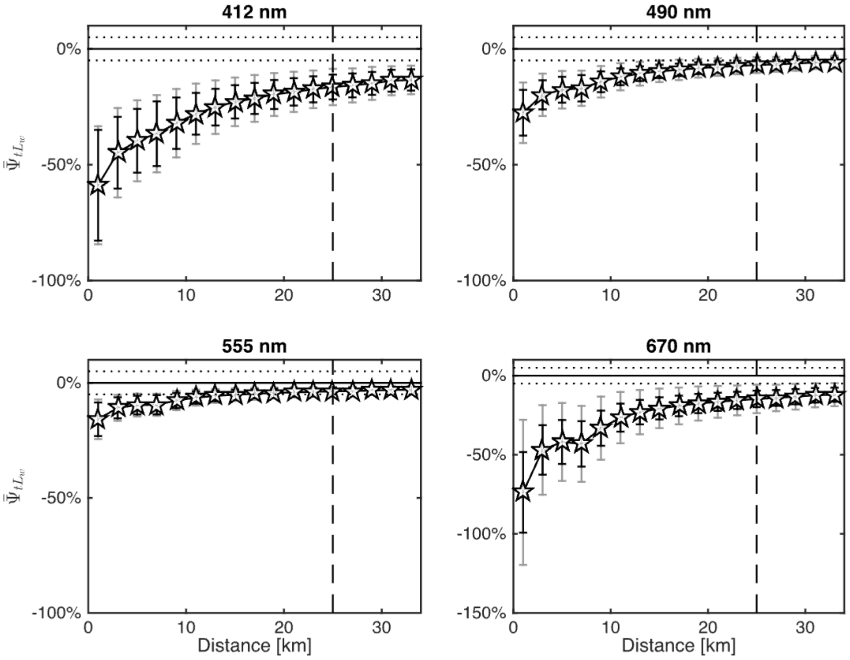

Source: (Bulgarelli et al., 2017)

The investigation was completed by evaluating the impact of AE on satellite primary products through match-ups of in situ and cloud-free SeaWiFS sample images (Bulgarelli et al., 2018).

The validation exercise was performed with the NASA SeaWiFS Data Analysis System (SeaDAS version 7; https://seadas.gsfc.nasa.gov/), alternatively ingesting original SeaWiFS data and SeaWiFS data corrected at TOA for NAUSICAA estimated adjacency contributions, and alternatively including or excluding the default turbid water (TW) correction algorithm (Bailey et al., 2010). The analysis suggests AE exceeding TW contributions at NIR in the vast majority of cases between March and October, as well as indicates an overestimate of the water signal in the NIR by the standard SeaDAS procedure (likely imputable to the inability of the optical model implemented in the TW correction algorithm to reproduce actual bio-optical conditions at the AAOT) partially compensating adjacency perturbations.

The exercise showed biases decreasing at all wavelengths and throughout the year when correcting for the sole AE.

Notably, the exercise allowed explaining the observed intra-annual variation in biases of SeaWiFS primary products acquired at the AAOT in the period 2002-2010 (Zibordi et al., 2012) as a consequence of residual perturbations from uncompensated AE in data acquired in summer, and misinterpretation of NIR atmospheric signal as water contributions in data acquired in winter.

5.2 JRC analysis of adjacency effects in satellite data and satellite data products in coastal regions

NAUSICAA was further applied to evaluate the spatial extension of AE in typical coastal environments and for representative atmospheric, illumination and observational conditions (Bulgarelli and Zibordi, 2018a) (Fig. 23). Average values of $\xi_{L_{tot}}$ at representative OC center-wavelengths for different land covers are illustrated in Fig. 24.

Figure 23. Geometry of illumination and observation adopted in the simulations. The grey horizontal line represents the study transect.

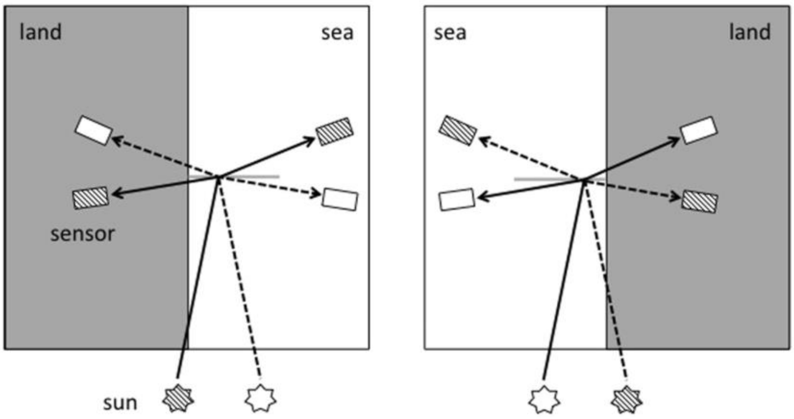

Source: (Bulgarelli and Zibordi, 2018a)

Figure 24. Values of $|\bar{\xi}_{L_{tot}}|$ at representative center-wavelengths along the study transect of Fig. 23 as a function of the distance from the coast for northern Adriatic Sea Case-2 moderately sediment-dominated waters and different land covers. Error bars represent uncertainties computed assuming uncorrelated contributions. Horizontal lines indicate the spectral NL values for the various sensors (SWF stands for SeaWiFS, MOD for MODIS, MER for MERIS).

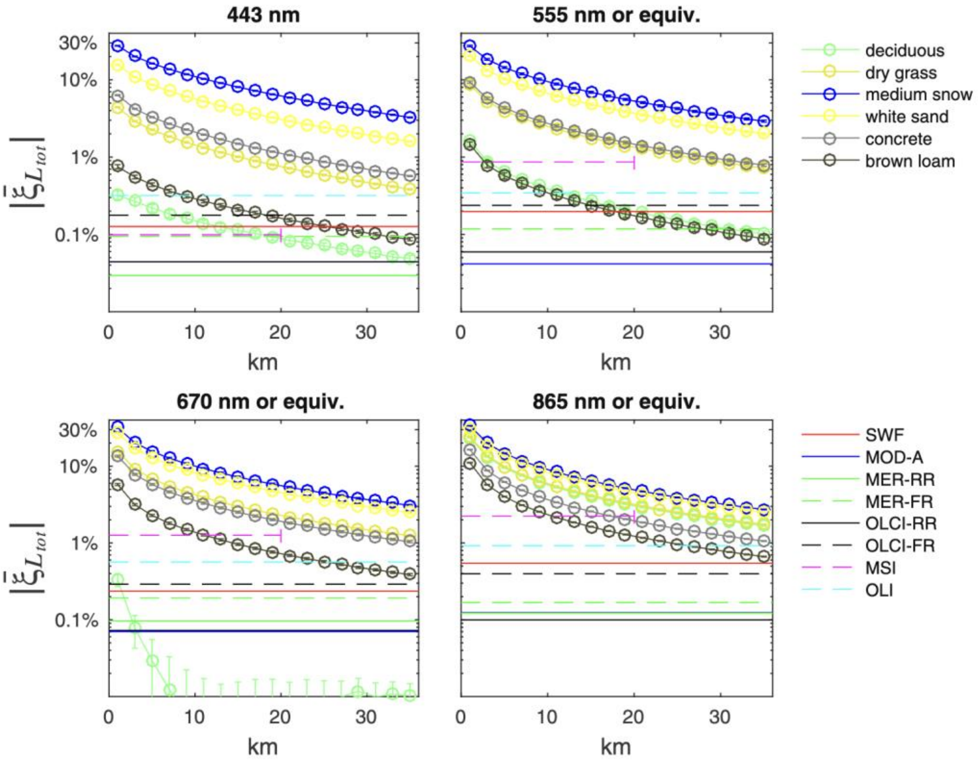

Source: (Bulgarelli and Zibordi, 2018a)

Fig. 25 shows biases ψ_{tL_w} induced by AE on tL_w retrieved with an AC-2 scheme. Results are for northern Adriatic Sea waters (i.e., Case-2 moderately sediment-dominated waters) and representative land covers along the study transect of Fig. 23. Over- and underestimated radiance observed at the coast might well exceed ± 100% at 443 nm in the presence of snow and green vegetation, respectively. Notably, misestimates might increase about 4 times in water dominated by CDOM, like those of the Baltic Sea (not shown).

Overall, the analysis of adjacency perturbations on satellite radiometric products from an AC scheme deriving the aerosol properties from the NIR showed that (Bulgarelli and Zibordi, 2018a): *i)* adjacency perturbations on the satellite-derived atmospheric radiance are not only correlated to the strength of the land albedo in the NIR, but to its spectral dependence, too; *ii)* AE in the NIR (affecting the retrieval of the atmospheric radiance) might compensate adjacency perturbations at visible wavelengths, so that even biases on the retrieved water-leaving radiance are not directly correlated to the strength of the land spectral albedo. For example, the impact of AE on the water signal retrieved at blue wavelengths might be larger for a vegetation land cover than for the more highly reflective concrete or white sand. Compensations might even occur in the presence of snow.

Figure 25. Values of the bias induced by AE on the derived water-leaving radiance at TOA, ψ_{tLw}, at representative wavelengths along the study transect of Fig. 23 as a function of the distance from the coast for northern Adriatic Sea waters and representative land covers (see legend of Fig. 24). Error bars indicate ± 1 standard deviation (N = 24 test cases).

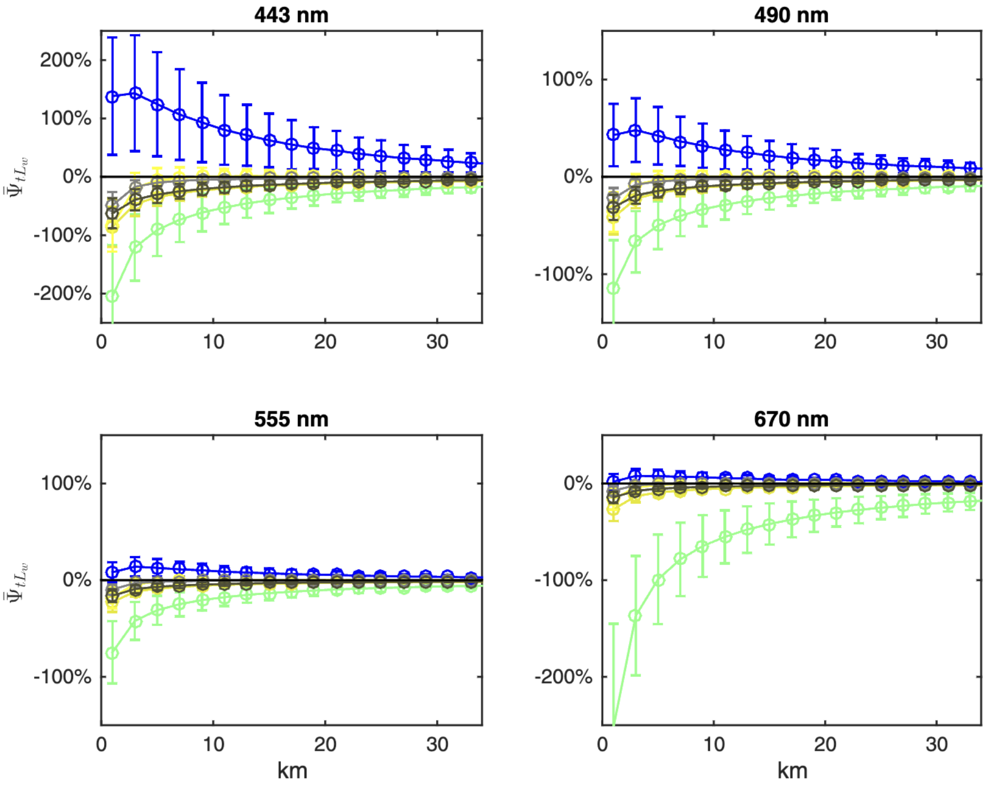

Source: (Bulgarelli and Zibordi, 2018a)

5.3 JRC contribution to the evaluation of adjacency effects at SVC sites

The NAUSICAA code was employed to theoretically investigate potential AE in marine data acquired by the OLCI instrument onboard the Sentinel-3 Copernicus space mission, when considering a conjectural SVC infrastructure located in the Sicily Channel nearby the small Lampedusa island (approximately 2.5 km by 12 km) (Bulgarelli and Zibordi, 2020).

The analysis evidenced extremely different adjacency patterns (see Fig. 26) in the northern and southern water regions. North of the island (i.e., in the anti-solar plane) AE mainly derive from sky- and sun-glint contributions masked by the island itself, displaying slightly negative values which decrease with wavelength. South of the island AE is mostly dominated by land radiance contributions, with the highest values at 865 nm, where they reach up to 40% at the coast, remaining larger than the sensor NL up to about 8 and 14 km for OLCI FR and OLCI RR data, respectively. Beyond such distances from the coast, AE was estimated to not affect the 5% uncertainty requirement for the water-leaving radiance in the blue-green spectral regions.

Figure 26. Percent contribution of adjacency effects ξ_{Ltot} to the top-of-atmosphere radiance at 865 nm over 140x140 surface square elements 200 m wide centred on the island, determined for typical observation and land - water optical properties. The white straight lines indicate transects matter of extensive investigations. The yellow and red contour lines identify the noise level for OLCI Full-Resolution and OLCI Reduced-Resolution, respectively. Dashed and continuous contour lines indicate negative and positive values of the sensor noise level, respectively.

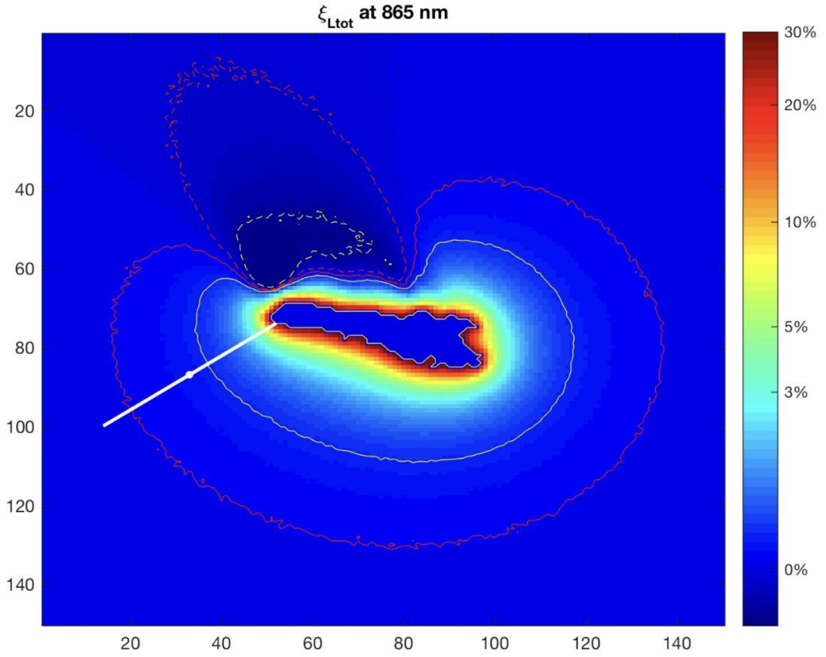

Source: (Bulgarelli and Zibordi, 2020)

5.4 JRC analysis of adjacency effects in inland waters

Adjacency effects are expected to increase in inland water basins, since these are surrounded by land. Lake Maggiore was selected as a test case to perform NAUSICAA simulations of average $\xi_{L_{tot}}$ in typical OC acquisitions. Results depicted in Fig. 27 were obtained for average atmospheric, illumination and observation conditions. They show values of $\xi_{L_{tot}}$ exceeding typical OC sensors' NL (Bulgarelli and Zibordi, 2018a) even at the centre of the lake, and particularly in the NIR (Bulgarelli, 2024a).

Figure 27. Adjacency contribution at the sensor ξ_{Ltot} (percent values, note that the scale is different for the different wavelengths). Inlet plots depict ξ_{Ltot} along the transect indicated in the pictures.

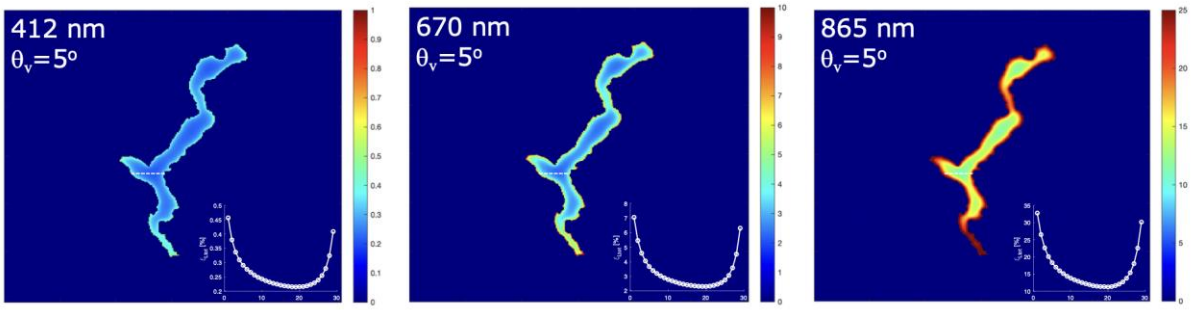

Source: Bulgarelli, 2024a

6 Conclusions

The NAUSICAA 3D MC code, whose accuracy and computational efficiency were carefully evaluated, belongs to the JRC's ARTEMIS-OC software suite for the simulation of the signal at OC satellite and in-situ sensors in support to the Copernicus program for Earth observation, monitoring and safeguarding.

In specific, NAUSICAA represents a powerful and versatile tool to evaluate perturbations from nearby land in OC data of coastal and inland waters, the so-called adjacency effects.

The present report illustrated the methodology applied in NAUSICAA, discussed the accuracy of simulated results and the code computational efficiency, described inputs and outputs, and summarised main applications.

NAUSICAA was extensively applied to assess adjacency perturbations in realistic OC satellite observations of coastal and inland waters.

Based on NAUSICAA simulations (Bulgarelli et al., 2014; 2017; 2018c; Bulgarelli and Zibordi, 2018a; 2018b), it was possible to draw the following general considerations:

- urgent ad clear need to account for AE when processing OC data from coastal and inland water regions
- modeling and correction of AE should account for:
  - sensor viewing angle (AE significantly increase with the viewing angle, nearly doubling from 20° to 50°);
  - illumination conditions (AE appreciably decrease with the solar zenith angle)
  - atmospheric conditions—there is evidence that, at some distance from the coast, the phenomenon is Rayleigh-dominated;
  - when the contrast between water and land is low (as for green vegetation, bare soil and cropland at the blue wavelengths), relevance should be given to the optical properties of the water;
  - when the contrast between land and water is high (as for all land covers at NIR and for snow, white sand, dry vegetation and concrete at all wavelengths), the optical properties of the water and its surface are not crucial in the determination of the AE
- AE needs to be considered when selecting the location of a site for the vicarious calibration of Copernicus products: the site should be put at a safe distance from the coast to avoid AE, or, alternatively, the utilised atmospheric correction code should account for AE.

Results obtained from the NAUSICAA code contributed to raise awareness on the need to correct for land perturbations in OC remote sensing.

The handling of AE is accounted for in the specifications of CEOS Analysis Ready Data (ARD) of aquatic reflectance (Dekker et al., 2025).

References

Antoine, D., Morel, A., 1999. A multiple scattering algorithm for atmospheric correction of remotely sensed ocean colour (MERIS instrument): Principle and implementation for atmospheres carrying various aerosols including absorbing ones. Int. J. of Remote Sensing 20, 1875–1916. https://doi.org/10.1080/014311699212533

Bailey, S.W., Franz, B.A., Werdell, P.J., 2010. Estimation of near-infrared water-leaving reflectance for satellite ocean color data processing. Opt Express 18, 7521. https://doi.org/10.1364/oe.18.007521

Bélanger, S., Ehn, J.K., Babin, M., 2007. Impact of sea ice on the retrieval of water-leaving reflectance, chlorophyll a concentration and inherent optical properties from satellite ocean color data. Remote Sens Environ 111, 51–68. https://doi.org/10.1016/j.rse.2007.03.013

Bulgarelli, B., Vitale, G., Advanced Radiative Transfer Models for the simulation of In situ and Satellite Ocean Color data (ARTEMIS - OC) : the Propagating Environment for Radiance Simulations in atmosphEre and wAter (PERSEA) code, JRC report in preparation

Bulgarelli, B., 2024. Advanced Radiative Transfer Models for the simulation of In situ and Satellite Ocean Color data (ARTEMIS - OC) : the Finite Element Method (FEM) numerical code (No. JRC 135763). Publications Office of the European Union, Luxembourg.

Bulgarelli, B., 2023. Advanced Radiative Transfer Models for the simulation of In situ and Satellite Ocean Color data (ARTEMIS-OC): the Finite Element Method (FEM) numerical code. Publications Office of the European Union, Luxembourg.

Bulgarelli, B., Kiselev, V., Zibordi, G., 2017. Adjacency effects in satellite radiometric products from coastal waters: a theoretical analysis for the northern Adriatic Sea. applied optics 56, 854–16. https://doi.org/10.1364/ao.56.000854

Bulgarelli, B., Kiselev, V., Zibordi, G., 2014. Simulation and analysis of adjacency effects in coastal waters: a case study. Applied optics 53, 1523–1545. https://doi.org/10.1364/ao.53.001523

Bulgarelli, B., Kisselev, V.B., Roberti, L., 1999. Radiative transfer in the atmosphere-ocean system: the finite-element method. applied optics 38, 1530–1542. https://doi.org/10.1364/ao.38.001530

Bulgarelli, B., Zibordi, G., 2020. Adjacency radiance around a small island: implications for system vicarious calibrations. applied optics 59, C63–C69. https://doi.org/10.1364/ao.378512

Bulgarelli, B., Zibordi, G., 2018a. On the detectability of adjacency effects in ocean color remote sensing of mid-latitude coastal environments by SeaWiFS, MODIS-A, MERIS, OLCI, OLI and MSI. Remote Sensing of Environment 209, 423–438. https://doi.org/10.1016/j.rse.2017.12.021

Bulgarelli, B., Zibordi, G., 2018b. Seasonal Impact of Adjacency Effects on Ocean Color Radiometry at the AAOT Validation Site. Geoscience and Remote Sensing Letters, IEEE 15, 488–492. https://doi.org/10.1109/lgrs.2017.2781900

Bulgarelli, B., Zibordi, G., Mélin, F., 2018. On the minimization of adjacency effects in SeaWiFS primary data products from coastal areas. Opt. Express 26, A709. https://doi.org/10.1364/oe.26.00a709

Cox, C., Munk, W., 1954. Measurement of the roughness of the sea surface from photographs of the sun's glitter. J Opt Soc Amer 44.

D'Alimonte, D., Zibordi, G., Kajiyama, T., Cunha, J.C., 2010. Monte Carlo code for high spatial resolution ocean color simulations. applied optics 49, 4936. https://doi.org/10.1364/ao.49.004936

Dekker, A., Evers-King, H. , Bulgarelli, B. , Gurlin, D., Gege, P., Pinnel, N., Brockmann, C. , Costa, M., Stroble, P., Shukla, T., Steventon, M., Jones, H., "The CEOS ARD for Aquatic Reflectance – Evolving From Inland and Near-Coastal Waters to Include Oceans" submitted to Living Planet Symposium 2025, Wien (A)

Deschamps, P.Y., Herman, M., Tanre, D., 1983. Definitions of atmospheric radiance and transmittances in remote sensing. Remote Sensing of Environment 13, 89–92. https://doi.org/10.1016/0034-4257(83)90029-9

Doyle, J.P., Rief, H., 1998. Photon transport in three-dimensional structures treated by random walk techniques: Monte Carlo benchmark of ocean colour simulations. Mathematics and Computers in Simulation 47, 215–241.

Gordon, H.R., 1985. Ship perturbation of irradiance measurements at sea 1: Monte Carlo simulations. Appl Optics 24, 4172. https://doi.org/10.1364/ao.24.004172

Gordon, H.R., Wang, M., 1994. Retrieval of water-leaving radiance and aerosol optical thickness over the oceans with SeaWiFS: a preliminary algorithm. applied optics 33, 443–452. https://doi.org/10.1364/ao.33.000443

Gordon, H.R., Wang, M., 1992. Surface-roughness considerations for atmospheric correction of ocean color sensors. I: The Rayleigh-scattering component. applied optics 31, 4247–4260. https://doi.org/10.1364/ao.31.004247

Hansen, J., Studies, G.I. for S., Center, G.S.F., Administration, U.S.N.A. and S., 1969. Exact and approximate solutions for multiple scattering by cloudy and hazy planetary atmospheres. Journal of the Atmospheric Sciences 26, 478–487.

van de Hulst, H.C., 1981. Light scattering by small particles. Courier Corporation.

Henyey, L.C., Greenstein, J.L., 1941. Diffuse radiation in the Galaxy. Astrophys. J. 93, 70. https://doi.org/10.1086/144246

Hu, C., Carder, K.L., Muller-Karger, F.E., 2001. How precise are SeaWiFS ocean color estimates? Implications of digitization-noise errors. Remote Sensing of Environment 76, 239–249.

Hu, C., Feng, L., Lee, Z., Davis, C.O., Mannino, A., McClain, C.R., Franz, B.A., 2012. Dynamic range and sensitivity requirements of satellite ocean color sensors: learning from the past. Appl Optics 51, 6045. https://doi.org/10.1364/ao.51.006045

Iwabuchi, H., 2006. Efficient Monte Carlo methods for radiative transfer modeling. Journal of the Atmospheric Sciences 63, 2324–2339.

Kajiyama, T., D'Alimonte, D., Cunha, J.C., 2016. A high-performance computing framework for Monte Carlo ocean color simulations. Concurrency Computat.: Pract. Exper. 29, e3860. https://doi.org/10.1002/cpe.3860

Kattawar, G.W., 1975. A three-parameter analytic phase function for multiple scattering calculations. Journal of Quantitative Spectroscopy and Radiative Transfer 15.9, 839–849.

Kaufman, Y.J., 1984. Atmospheric effect on spatial resolution of surface imagery. Applied optics 23, 3400–3408. https://doi.org/10.1364/ao.23.003400

Kaufman, Y.J., 1979. Effect of the Earth's atmosphere on contrast for zenith observation. J. Geophys. Res 84, 3165–3172.

Kiselev, V., Bulgarelli, B., Heege, T., 2015. Sensor independent adjacency correction algorithm for coastal and inland water systems. Remote Sensing of Environment 157, 85–95. https://doi.org/10.1016/j.rse.2014.07.025

Kisselev, V., Bulgarelli, B., 2004. Reflection of light from a rough water surface in numerical methods for solving the radiative transfer equation. Journal of Quantitative Spectroscopy and Radiative Transfer 85, 419–435. https://doi.org/10.1016/s0022-4073(03)00236-x

Kisselev, V.B., Roberti, L., Perona, G., 1995. Finite-element algorithm for radiative transfer in vertically inhomogeneous media: numerical scheme and applications. applied optics 34, 8460–8471. https://doi.org/10.1364/ao.34.008460

Kneizys, F.X., Shettle, E.P., Abreu, L.W., Chetwynd, J.H., Anderson, G.P., 1988. Users Guide to LOWTRAN 7. google.it.

Liou, K.-N., 2002. An Introduction to Atmospheric Radiation, Academic Press. Academic Press.

Lux I., and Koblinger, L., Monte Carlo particle transport methods: neutron and photon calculations. CRC Press, 1991.

Martonchik, J.V., Bruegge, C.J., Strahler, A.H., 2000. A review of reflectance nomenclature used in remote sensing. Remote Sensing Reviews 19, 9–20. https://doi.org/10.1080/02757250009532407

Mayer, B., Kylling, A., Emde, C., Hamann, U., Buras, R., 2011. libRadtran user's guide.

Mélin, F., Zibordi, G., Holben, B.N., 2013. Assessment of the Aerosol Products From the SeaWiFS and MODIS Ocean-Color Missions. Geoscience and Remote Sensing Letters, IEEE 10, 1185–1189. https://doi.org/10.1109/lgrs.2012.2235408

Mobley, C.D., 1994. Light and water: Radiative transfer in natural waters. Academic press San Diego 592.

Mobley, C.D., Werdell, J., Franz, B., Ahmad, Z., Bailey, S., 2016. Atmospheric Correction for Satellite Ocean Color Radiometry, NASA. NASA.

Monahan, E.C., O'Muircheartaigh, I.G., 1986. Whitecaps and the passive remote sensing of the ocean surface. Int. J. of Remote Sensing 7, 627–642. https://doi.org/10.1080/01431168608954716

Otterman, J., Fraser, R.S., 1979. Adjacency effects on imaging by surface reflection and atmospheric scattering: cross radiance to zenith. Applied optics 18, 2852–2860. https://doi.org/10.1364/ao.18.002852

Pan, Y., Bélanger, S., 2024. Genetic Algorithm for Atmospheric Correction (Gaac) of Water Bodies Impacted by Adjacency Effects. https://doi.org/10.2139/ssrn.4867699

Paulino, R.S., Martins, V.S., Novo, E.M.L.M., Barbosa, C.C.F., Carvalho, L.A.S. de, Begliomini, F.N., 2022. Assessment of Adjacency Correction over Inland Waters Using Sentinel-2 MSI Images. Remote. Sens. 14, 1829. https://doi.org/10.3390/rs14081829

Pearce, W.A., 1986. Monte Carlo study of the atmospheric spread function. Optical Society of America 25, 438–447. https://doi.org/10.1364/ao.25.000438

Pinty, B., Lattanzio, A., Martonchik, J.V., Verstraete, M.M., Gobron, N., Taberner, M., Widlowski, J.-L., Dickinson, R.E., Govaerts, Y., 2005. Coupling Diffuse Sky Radiation and Surface Albedo. Journal of the Atmospheric Sciences 62, 2580–2591. https://doi.org/10.1175/jas3479.1

Pinty, B., Widlowski, J.-L., Gobron, N., Verstraete, M.M., Diner, D.J., 2002. Uniqueness of Multiangular Measurements—Part I: An Indicator of Subpixel Surface Heterogeneity from MISR. Ieee T Geosci Remote 40, 1560. https://doi.org/10.1109/tgrs.2002.801148

Potter, J.F., 1970. The Delta Function Approximation in Radiative Transfer Theory. J Atmos Sci 27, 943–949. https://doi.org/10.1175/1520-0469(1970)027<0943:tdfair>2.0.co;2

Preisendorfer, R.W., 1976. Hydrologic Optics. Pacific Mar. Environ. Lab/NOAA, Seattle, WA.

Prokhorov, A.V., 1998. Monte Carlo method in optical radiometry. Metrologia 35, 465–471. https://doi.org/10.1088/0026-1394/35/4/44

Rahman, H., Verstraete, M.M., Pinty, B., 1993. Coupled surface-atmosphere reflectance (CSAR) model: 1. Model description and inversion on synthetic data. J. Geophys. Res 98, 20779. https://doi.org/10.1029/93jd02071

Reinersman, P.N., Carder, K.L., 1995. Monte Carlo simulation of the atmospheric point-spread function with an application to correction for the adjacency effect. Appl. Opt. 34, 4453. https://doi.org/10.1364/ao.34.004453

Roberti, L., 1997. Monte Carlo radiative transfer in the microwave and in the visible: biasing techniques 36, 7929–7938.

Robinson, I.S., 2004. Measuring the Oceans from Space, Springer Verlag. Springer Verlag.

Ruddick, K.G., Ovidio, F., Rijkeboer, M., 2000. Atmospheric correction of SeaWiFS imagery for turbid coastal and inland waters. Appl Optics 39, 897. https://doi.org/10.1364/ao.39.000897

Saltelli, A., Bammer, G., Bruno, I., Charters, E., Fiore, M.D., Didier, E., Espeland, W.N., Kay, J., Piano, S.L., Mayo, D., Pielke, R., Portaluri, T., Porter, T.M., Puy, A., Rafols, I., Ravetz, J.R., Reinert, E., Sarewitz, D., Stark, P.B., Stirling, A., Sluijs, J. van der, Vineis, P., 2020. Five ways to ensure that models serve society: a manifesto. 482–484.

Santer, R., Schmechtig, C., 2000. Adjacency effects on water surfaces: Primary scattering approximation and sensitivity study. Applied optics 39, 361–375. https://doi.org/10.1364/ao.39.000361

Sei, A., 2015. Efficient correction of adjacency effects for high-resolution imagery: integral equations, analytic continuation, and Padé approximants. Applied optics 54, 3748–11. https://doi.org/10.1364/ao.54.003748

Sei, A., 2007. Analysis of adjacency effects for two Lambertian half-spaces. Int. J. of Remote Sensing 28, 1873–1890. https://doi.org/10.1080/01431160600851868

Siqueira, A., Barnes, C., Labahn, S., Dekker, A., Bulgarelli, B., Brockmann, C., Gurlin, D., Ortiz, J.D., Ogashawara, I., Vodacek, A., Pahlevan, N., Keukelare, L. de, Reusen, I., Peters, S., Giardino, C., Kutser, T., Greb, S., Sterckx, S., Brando, V.E., Neely, M.-B., (NOAA), P.D., 2022. CEOS Analysis Ready Dara for Land _ Aquatic Reflectance (CARD4L-AR).

Spanier, J. and Gelbard, E. M., Monte Carlo Principles and Neutron Transport Problems, ser. Addison-Wesley series in computer science and information processing. Addison-Wesley, 1969.

Stamnes, K., Tsay, S.-C., Wiscombe, W., Jayaweera, K., 1988. Numerically stable algorithm for discrete-ordinate-method radiative transfer in multiple scattering and emitting layered media. Applied optics 27, 2502–2509. https://doi.org/10.1364/ao.27.002502

Sterckx, S., Knaeps, E., Ruddick, K., 2011. Detection and correction of adjacency effects in hyperspectral airborne data of coastal and inland waters: the use of the near infrared similarity spectrum. Int. J. Remote Sens. 32, 6479–6505. https://doi.org/10.1080/01431161.2010.512930

Storch, T., Honold, H.-P., Chabrillat, S., Habermeyer, M., Tucker, P., Brell, M., Ohndorf, A., Wirth, K., Betz, M., Kuchler, M., Mühle, H., Carmona, E., Baur, S., Mücke, M., Löw, S., Schulze, D., Zimmermann, S., Lenzen, C., Wiesner, S., Aida, S., Kahle, R., Willburger, P., Hartung, S., Dietrich, D., Plesia, N., Tegler, M., Schork, K., Alonso, K., Marshall, D., Gerasch, B., Schwind, P., Pato, M., Schneider, M., Reyes, R. de los, Langheinrich, M., Wenzel, J., Bachmann, M., Holzwarth, S., Pinnel, N., Guanter, L., Segl, K., Scheffler, D., Foerster, S., Bohn, N., Bracher, A., Soppa, M.A., Gascon, F., Green, R., Kokaly, R., Moreno, J., Ong, C., Sornig, M., Wernitz, R., Bagschik, K., Reintsema, D., Porta, L.L., Schickling, A., Fischer, S., 2023. The EnMAP imaging spectroscopy mission towards operations. Remote. Sens. Environ. 294, 113632. https://doi.org/10.1016/j.rse.2023.113632

Tanre, D., Herman, M., Deschamps, P.Y., Leffe, A. de, 1979. Atmospheric Modeling For Space Measurements Of Ground Reflectances, Including Bidirectional Properties. Applied optics 18, 3587–3594. https://doi.org/10.1364/ao.18.003587

Vermote, E.F., Vermeulen, A., 1999. Atmospheric correction algorithm: spectral reflectances (MOD09), ATBD version. ATBD version.

Wenzel, J., Kiselev, V., Heege, T., Bachmann, M., Richter, R., 2022. EnMAP Ground SegmentLevel 2A Processor(Atmospheric Correction Water) ATBD - EN-PCV-TN-6008 issue 3.1, EN-PCV-TN-6008 issue 3.1.

Wu, Y., Knudby, A., Lapen, D., 2023. Topography-adjusted Monte Carlo simulation of the adjacency effect in remote sensing of coastal and inland waters. J. Quant. Spectrosc. Radiat. Transf. 303, 108589. https://doi.org/10.1016/j.jqsrt.2023.108589

Wu, Y., Knudby, A., Pahlevan, N., Lapen, D., Zeng, C., 2024. Sensor-generic adjacency-effect correction for remote sensing of coastal and inland waters. Remote Sens. Environ. 315, 114433. https://doi.org/10.1016/j.rse.2024.114433

Yang, H., Gordon, H.R., 1997. Remote sensing of ocean color: assessment of water-leaving radiance bidirectional effects on atmospheric diffuse transmittance. Applied Optics LP 36, 7887–7897. https://doi.org/10.1364/ao.36.007887

Zhao, Y., He, X., Bai, Y., Xu, F., Jin, X., Li, T., Wang, D., Gong, F., 2024. Adjacency Effect on Rayleigh Scattering Radiance for Satellite Remote Sensing of River Waters. IEEE Trans. Geosci. Remote Sens. 62, 1–20. https://doi.org/10.1109/tgrs.2024.3487906

Zibordi, G., Berthon, J.F., Doyle, J.P., Grossi, S., Linde, D. van der, Targa, C., Alberotanza, L., 2002. Coastal Atmosohere and Sea Time Series (CoASTS), Part 1: A tower-based, long-term measurement program. NASA Technical Memorandum - SeaWIFS Postlaunch Technical Report Series 1–29.

Zibordi, G., Holben, B., Mélin, F., D'Alimonte, D., Berthon, J.F., Slutsker, I., Giles, D., 2010. AERONET-OC: an overview. Canadian Journal of Remote Sensing 36, 488–497. https://doi.org/10.5589/m10-073

Zibordi, G., Holben, B.N., Talone, M., D'Alimonte, D., Slutsker, I., Giles, D.M., Sorokin, M.G., 2021. Advances in the Ocean Color Component of the Aerosol Robotic Network (AERONET-OC). J Atmos Ocean Tech 38, 725–746. https://doi.org/10.1175/jtech-d-20-0085.1

Zibordi, G., Mélin, F., Berthon, J.F., 2012. Intra-annual variations of biases in remote sensing primary ocean color products at a coastal site. Remote Sensing of Environment 124, 627–636. https://doi.org/10.1016/j.rse.2012.06.016

Zibordi, G., Mélin, F., Berthon, J.-F., Holben, B., Slutsker, I., Giles, D., D'Alimonte, D., Vandemark, D., Feng, H., Schuster, G., Fabbri, B.E., Kaitala, S., Seppälä, J., 2009. AERONET-OC: A Network for the Validation of Ocean Color Primary Products. J Atmos Ocean Tech 26, 1634–1651. https://doi.org/10.1175/2009jtecho654.1

Zibordi, G., and Berthon, J.-F., 2024. Coastal Atmosphere and Sea Time Series (CoASTS) and Bio-Optical mapping of Marine Properties (BiOMaP): The CoASTS-BiOMaP dataset. *Earth System Science Data*, *16*(12), 5477–5502. https://doi.org/10.5194/essd-16-5477-2024

List of abbreviations and definitions

Abbreviations	Definitions
3D	Three-dimensional
AAOT	Aqua Alta Oceanographic Tower
AC	Atmospheric Correction
AE	Adjacency Effects
AERONET-OC	Ocean Color component of the Aerosol Robotic Network
AquaFEM	FEM configuration for the simulation of the in-water light field
ARD	Analysis Ready Data
ARTEMIS-OC	Advanced Radiative Transfer Models for In Situ and Satellite Ocean Color data
BRDF	Bidirectional radiance distribution function
C3S	Climate Change Service
CDOM	Color Dissolved Organic Matter
CEOS	Committee on Earth Observation Satellites
CMEMS	Copernicus Marine Environment Monitoring Service
DHR	directional–hemispherical reflectance
ECV	Essential Climate Variable
EO	Earth Observation
EOSS	Earth Observation Support to Copernicus Climate and Marine Services
EnMAP	Environmental Mapping and Analysis Program
EUMETSAT	European Organisation for the Exploitation of Meteorological Satellites

Abbreviations	**Definitions**
FEM	Finite Element Method code
FEMrad-OC	FEM configuration for the simulation of the radiance at Ocean Color satellite sensors
FR	Full-resolution
GCOS	Global Climate Observation System
GOOS	Global Ocean Observing System
HR	High Resolution
LR	Low Resolution
MC	Monte Carlo
MERIS	Medium Resolution Imaging Spectrometer
MODIS	*Moderate Resolution Imaging Spectrometer*
NASA	National Aeronautics and Space Administration
NAUSICAA	Novel Adjacency Perturbation Simulator for Coastal Areas
NEΔL	Noise Equivalent Radiance Difference
NIR	Near Infrared
NL	Noise Level
OC	Ocean Color
OLCI	Ocean and Land Colour Instrument
OLI	Operational Land Imager
PERSEA	Propagating Environment for Radiance Simulations in atmosphEre and wAter
RR	Reduced-resolution
RTE	radiative transfer equation

Abbreviations	Definitions
RTM	radiative transfer model
SeaDAS	radiative transfer model
SeaWiFS	Sea Wide Field of View Sensor
SkyFEM	FEM configuration for the simulation of the Sky-radiance
SVC	System Vicarious Calibration
TOA	Top of Atmosphere
TTHG	Two-terms Henyey-Greenstein
TW	Turbid water
SNR	Sensor to noise ratio
SVC	System Vicarious Calibration
Abbreviations	Definitions
ΑΒΓ	Alpha Beta Gamma
ΔΕΖ	Delta Epsilon Zeta Delta Epsilon Zeta Delta Epsilon Zeta Delta Epsilon Zeta Delta Epsilon Zeta Delta Epsilon Zeta
ΗΘΙ	Eta Theta Iota

List of figures

List of tables

Annexes

Annex 1. Input variables to the main subroutine *NAUSICAA_RTE_solver.f*

Input variables of subroutine *NAUSICAA_RTE_solver.f* are divided into hard coded variables (Table 3) and variables passed to the subroutine (Table 4). In both tables, code variable names are listed, together with their type, scientific symbol (when appropriate) and short description.

Table 3 Hard-coded variables (I stands for integer, R for real and L for logical)

Variable	***Type***	***Symbol***	***Description***
ISEED	I		arbitrary integer for the initialisation of the random generating function prior its first call
NREF	R	n	air-water refraction index. Default: NREF = 1.34
WIND	R	v_w	wind speed [m*sec-1]. Default: WIND = 3.3 m/s
TRES-RR	R		threshold for the application of the Russian roulette on weight. Default: TRES_RR = 0.2 (not used)
NSTEP	I		number of points in each cell at which the solution is computed (not used)

Source: (Bulgarelli et al., 2025)

Hard coded is also the name of the file containing the tabulated DHR data for the wind-roughened sea surface. Example: DHR_3.3.DAT for wind speed WIND = 3.3m/s. Data are for opposite incident direction (viewing direction). WARNING: if the wind speed is changed the corresponding DHR file must be read!

Table 4 Variables passed to the *NAUSICAA_RTE_solver* subroutine (I stands for integer, R for real and L for logical)

Variable	***Type***	***Symbol***	***Description***
photons			
NPHO	I	N_{pho}	Number of backward photons started from the sensor
TRES	R		threshold below which photons life is considered to be extinguished.
Illumination conditions			
SUNCOS	R	$cos\theta_{sunbeam}$	cosine of the incident sunbeam polar angle. For sun is at nadir, SUNCOS= -1.0
SUNAZ	R	$\phi_{sunbeam}$	Incident sunbeam azimuthal angle in degrees anticlockwise from the x-axis
SOCO	R	F_0/π	Intensity of the incident parallel beam on the top boundary in arbitrary units. It is such that SOCO·π = incident flux.

Output radiance direction			
MXUMU	I		Maximum number of output radiance polar angles
NUMU	I		Number of output radiance polar angles
UMU(MXUMU)	R	$cos\theta$	Cosine of the output radiance polar angle. UMU(Nadir) =1.0.
AZIM	R	ϕ	output radiance azimuth angle in degrees anticlockwise from the X direction. AZIM=0 in the X direction
Output height			
POSZ	R		Height in [km] at which the solution is computed, i.e., sensor height. POSZ=0 surface level.
Target surface element			
minLLL,maxLLL	I		First and last target element in the x-direction
minMMM,maxMMM	I		First and last target element in the y-direction
Surface definition			
MXCL	I		Maximum number of elements in the x- and y- direction.
NXCL	I		Number of elements in the x-direction
NYCL	I		Number of elements in the y-direction
SIZE	R		Size of the square surface elements [km]
STEP	R		Distance [km] along the x- and y- direction between the computational points in which the intensity is computed inside each column. **NOTE: if not used must be set equal to SIZE**
NSTEP	I		Number of steps
ALBE(0:MXCL,0:MXCL)	R		Albedo of the Lambertian surface elements. It can range from 0 to 1. If set to 99.9 the surface element is assumed to be a water surface roughened by the wind.
LAMBERT(0:MXCL,0:MXCL)	L		.true. for Lambertian surface elements If .false. the surface is assumed to be characterized by a BRDF
Atmosphere definition			

MXLYR	I		Maximum number of vertical layers.
NLYR(0:MXCL,0:MXCL)	I		Number of vertical cells for each column
LYRHGT(0:MXCL,0:MXCL,0:MXLYR)	R		Top boundary of each cell [km]
KEXT(0:MXCL,0:MXCL,MXLYR)	R		Extinction coefficient for each cell
SALB(0:MXCL,0:MXCL,MXLYR)	R	ω_0	Single scattering albedo for each cell
AERSCPROB(0:MXCL,0:MXCL,MXLYR)		P_{aer}^{sc}	Aerosol scattering probability for each cell
MEANFP(0:MXCL,0:MXCL,MXLYR)			Mean free path for each cell = 1/KEXT
HENYEY	L		If .true., the phase function is TTHG If .flase. the phase function is read from FILEPHA
ASYM1(0:MXCL,0:MXCL,MXLYR), **ASYM2(0:MXCL,0:MXCL,MXLYR),** **ASYM3(0:MXCL,0:MXCL,MXLYR)**	R	g_1 g_2 as	TTHG asymmetry parameters for each cell
		Phase function	
MXAN	I		Maximum number of points for the tabulation of the phase function. The points are angles in degrees. MXAN is set equal to 180 in this version of the program. The numeration starts from 0 for a total of 181.
ANG(0:MXAN)	R		Tabulated angles for the phase function
NANG	I		Number of points for the tabulation of the phase function
PHA (0:MXCL,0:MXCL,MXLYR,0:MXAN)	R	$\tilde{\beta}_{aer}$	Values of the phase function at tabulated angles
PHADI(0:MXCL,0:MXCL,MXLYR,0:MXAN)	R		cumulative distribution of the input function

Source: (Bulgarelli et al., 2025)

Getting in touch with the EU

In person

All over the European Union there are hundreds of Europe Direct centres. You can find the address of the centre nearest you online (european-union.europa.eu/contact-eu/meet-us_en).

On the phone or in writing

Europe Direct is a service that answers your questions about the European Union. You can contact this service:

— by freephone: 00 800 6 7 8 9 10 11 (certain operators may charge for these calls),

— at the following standard number: +32 22999696,

— via the following form: european-union.europa.eu/contact-eu/write-us_en.

Finding information about the EU

Online

Information about the European Union in all the official languages of the EU is available on the Europa website (european-union.europa.eu).

EU publications

You can view or order EU publications at op.europa.eu/en/publications. Multiple copies of free publications can be obtained by contacting Europe Direct or your local documentation centre (european-union.europa.eu/contact-eu/meet-us_en).

EU law and related documents

For access to legal information from the EU, including all EU law since 1951 in all the official language versions, go to EUR-Lex (eur-lex.europa.eu).

EU open data

The portal data.europa.eu provides access to open datasets from the EU institutions, bodies and agencies. These can be downloaded and reused for free, for both commercial and non-commercial purposes. The portal also provides access to a wealth of datasets from European countries.